Anatomy of continuous Mars SEIS and pressure data from unsupervised learning

Salma Barkaoui, Philippe Lognonné, Taichi Kawamura, Éléonore Stutzmann, Léonard Seydoux, Maarten de Hoop, Randall Balestriero, John-Robert Scholz, Grégory Sainton, Matthieu Plasman, et al.

Anatomy of continuous Mars SEIS and Pressure data from unsupervised learning

Salma Barkaoui[1†], Philippe Lognonné[1‡], Taichi Kawamura[1§], Éléonore Stutzmann[1¶], Léonard Seydoux[2‖], Maarten De Hoop[3∗∗], Randall Balestriero[3††], John-Robert Scholz[4‡‡], Grégory Sainton[1Ⓢ], Matthieu Plasman[1θ], Savas Ceylan[5], John Clinton[10∗▽], Aymeric Spiga[6□], Rudolf Widmer-Schnidrig[8⊕], Francesco Civilini[9○], W.Bruce Banerdt[7⊗]

[1]Université de Paris, Institut de physique du globe de Paris, CNRS F-75005 Paris, France.

[2]Institut des sciences de la Terre, Université Grenoble-Alpes, UMR CNRS 5375, France.

[3]Rice University, Houston, TX, USA.

[4]Max Planck Institute for Solar System Research, Göttingen, Germany.

[5]Institute for Geophysics, ETH Zürich, Zürich, Switzerland.

[6]Laboratoire de Météorologie Dynamique/Institut Pierre Simon Laplace (LMD/IPSL), Sorbonne Université, Centre National de la Recherche Scientifique (CNRS), France.

[7]Jet Propulsion Laboratory, California Institute of Technology, Pasadena, CA 91109, USA.

[8]University of Stuttgart, Institute of geodesy, Stuttgart, Germany

[9]NASA's Marshall Space Flight Center

[10]Swiss Seismological Service, ETH Zürich, Zürich, Switzerland

- **Declaration of competing interests:** The authors declare that there is no conflict of interest.
- **Corresponding author:** Salma Barkaoui, email: barkaoui@ipgp.fr

[†]Salma Barkaoui: barkaoui@ipgp.fr
[‡]Philippe Lognonné: lognonne@ipgp.fr
[§]Taichi Kawamura: kawamura@ipgp.fr
[¶]Éléonore Stutzmann: stutz@ipgp.fr
[‖]Léonard Seydoux: leonard.seydoux@univ-grenoble-alpes.fr
[∗∗]Maarten De Hoop:mvd2@rice.edu
[††]Randall Balestriero: andallbalestriero@gmail.com
[‡‡]scholz@mps.mpg.de
[Ⓢ]Grégory Sainton:sainton@ipgp.fr
[θ]Matthieu Plasman:plasman@ipgp.fr
Savas Ceylan: savas.ceylan@erdw.ethz.ch
[▽∗]John Clinton: jclinton@sed.ethz.ch
[□]Aymeric Spiga: aymeric.spiga@sorbonne-universite.fr
[⊕]Rudolf Widmer-Schnidrig: widmer@gis.uni-stuttgart.de
[○]Francesco Civilini: francesco.civilini@nasa.gov
[⊗]W.Bruce Banerdt: william.b.banerdt@jpl.nasa.gov

Abstract

The seismic noise recorded by the InSight (Interior Exploration using Seismic Investigations, Geodesy, and Heat Transport) seismometer (SEIS) has a strong daily quasi-periodicity and numerous transient micro-events, associated mostly with an active Martian environment with wind bursts, pressure drops, in addition to thermally-induced lander and instrument cracks. That noise is far from Earth's micro-seismic noise. Quantifying the importance of non-stochasticity and identifying these micro-events is mandatory for improving continuous data quality and noise analysis technics, including autocorrelation. Cataloguing these events has so far been made with specific algorithms and operator's visual inspection. We investigate here the continuous data with an unsupervised deep learning approach built on a deep scattering network. This leads to the successful detection and clustering of these micro-events as well as better determination of daily cycles associated to changes in the intensity and color of the background noise. We first provide a description of our approach and then present the learned clusters followed by a study of their origin and associated physical phenomena. We show that the clustering is robust over several martian days, showing distinct types of glitches that repeat at a rate of several tens per sol with stable time differences. We show that the clustering and detection efficiency for pressure drops and glitches is comparable to or better than manual or targeted detection techniques proposed to date, noticeably with an unsupervised approach. Finally, we discuss the origin of other clusters found, especially glitch sequences with stable time offsets which might generate artifacts in auto-correlation analyses. We conclude with presenting the potential of unsupervised learning for long-term space mission operations, in particular, for geophysical and environmental observatories.

Keywords: Martian events, clustering, detection, unsupervised learning, deep learning, scattering network.

1 Introduction

InSight (Interior Exploration using Seismic Investigations, Geodesy and Heat Transport) landed on Mars on November 26, 2018 (Banerdt et al., 2020), and deployed the SEIS (Seismic Experiment for Interior Structure) experiment on the ground (Lognonné et al., 2019). It records the Martian pressure with the APSS (Auxiliary Payload Sensors Suite) experiment (Banfield et al., 2018, 2020), and since February 2019, ground ac-

celeration with SEIS almost continuously, detecting marsquakes (Lognonné et al., 2020; Giardini et al., 2020) and transient atmospheric signals (Garcia et al., 2020; Kenda et al., 2020; Charalambous et al., 2021).

The SEIS background noise (Lognonné et al., 2020; Stutzmann et al., 2021) is much lower in amplitude than Earth's seismic noise (Peterson, 1993). Because of the surface installation, atmospheric activity and surface temperature drive the noise fluctuations (Lognonné et al., 2020; Charalambous et al., 2021), leading to a strong daily trend and a significant non-stochastic character. This is, for example, illustrated by the relation in occurrences in time of the transient thermally induced micro-tilts (also denoted glitches) with the SEIS recorded temperature, as already observed by Scholz et al. (2020). When not corrected, these glitches lead to artifacts in auto-correlation analyses, as demonstrated by Kim et al.(2021). During daytime, other frequent transients events are associated with pressure drops, analyzed and cataloged by Lorenz et al. (2020); Spiga et al. (2021) from pressure data analysis and modeled by Lognonné et al. (2020); Banerdt et al. (2020); Kenda et al. (2020). Mostly above 1Hz, lander shaking events are also frequent, especially at lander resonance frequencies (Ceylan et al., 2021).

All the required cataloging efforts in identifying these transient signals are time-consuming, which might be critical for long-duration operations. In addition, the methods developed by Scholz et al. (2020) for glitches cannot identify easily non-stochastic patterns in the signal, such as sequences of glitches with stable offset time. Furthermore, the non-stochasticity can also be related to predictable changes in the color of the noise spectrum, such as those related to the daily variation of the atmospheric turbulences, even if not associated with observable transient signals in the time domain.

This study aims to identify families of signals in the continuous data recorded by SEIS to better understand the structure of the continuous data and its non-stochasticity using artificial intelligence. The analysis presented, here, does not focus on the detection of rare (on the time scale of a sol) seismic events (Clinton et al., 2021), but investigates instrument or local (e.g. lander or instrument-related or environmental) sources, which might either generate single or repeating signals which are similar enough to be clustered. The associated clustering problem (Goodfellow et al., 2016) fits in an unsupervised learning framework in a feature space generated with a deep scattering network that has its roots in time-frequency analysis. The deep scattering network (Andén & Mal-

lat, 2014; Bruna & Mallat, 2013; Andén & Mallat, 2014) has been made learnable, which allows our analysis to be fully adapted to unknown conditions, including those of Mars. The original algorithm was developed by Seydoux et al. (2020) for Earth continuous seismic data. We modified it to detect and classify the transient signals in the VBB/SEIS continuous data (InSight Mars SEIS Data Service, 2019) or APSS pressure data (Mora, 2019). This work is the first study to apply deep learning on martian seismic. During the course of this work, another study was made with atmospheric Curiosity data Priyadarshini & Puri (2021).

In this article, we first introduce the deep learning strategy developed and applied on Earth. We then applied it to SEIS and pressure data. For SEIS, two analyses are made, the first to identify how much the signal can be clustered and the second to detect repeating signals in the noise. For pressure, only the first step is made.

Finally, we compare the timing of the cluster's events with those reported in the already published catalog (Ceylan et al., 2021; Scholz et al., 2020; Spiga et al., 2021; Lorenz et al., 2021). For single events like glitches and pressure drops, deep learning provides comparable (for glitches) or better (for pressure drops) detection results than the already published methods. This comparison depends of course on the various thresholds used by all techniques. More importantly, we show that unsupervised machine learning detects non-stochastics features, such as repeating series of glitches, and clusters the noise based on its color (or spectrum). This provides important feedback on the noise structure and a critical check on assumptions in scientific analysis, such as auto-correlations of the continuous data (Deng & Levander, 2020; Kim et al., 2021; Schimmel et al., 2021). This will also help to better understand the impact of the atmospheric turbulence on SEIS data.

2 Method

2.1 Machine learning in seismology

Machine learning is a powerful approach to statistical data analysis and has had wide-ranging success in various fields (Jordan & Mitchell, 2015) including seismology (e.g. Jia & Ma, 2017; Kong et al., 2018; Malfante et al., 2018; Hibert et al., 2019; Falcin et al., 2021; Seydoux et al., 2020). Here, we distinguish supervised from unsupervised ap-

proaches. In a supervised approach, the algorithm learns the mapping between data samples and labels from labeled, training data.

Lack of labeled data requires unsupervised strategies. Cluster analysis is a common strategy used in unsupervised learning (e.g. Géron, 2019). Even if depending on hyperparameter values, unsupervised learning, performs an information-based data analysis (Bergen & Beroza, 2018) not relying on former, human-based labeling of data. It can also reveal new classes, which is out of reach for supervised algorithms trained to recognize already-known classes. In the present study we focus on noise, adopt the unsupervised strategy and compare its efficiency on SEIS data with the existing catalogs. For future studies focusing on marsquakes, supervised learning (employing the recurrent scattering neural network) will be tested to automate the manual task performed by the Mars Quake Service (MQS) (Clinton et al., 2018) and possibly detect more events.

Selecting a relevant and stable representation of waveforms (or waveform features) is critical to the success of clustering since the temporal representation of waveforms is sensitive to small deformations (Andén & Mallat, 2014). In seismic applications, the features have commonly been handcrafted (signal energy, spectral content; see, e.g. Malfante et al., 2018) which implies having a priori knowledge of the data content. Here, we learn the relevant features, which is known as representation learning. The representation is formed by a learnable deep scattering network.

2.2 Deep scattering network

A deep scattering network extracts stable representations of continuous data. This network is built layerwise from wavelet transforms (convolutions), taking moduli and pooling, that is, decimation with prior low-pass filtering (see Fig 1 and Seydoux et al. (2020)).

The modulus of the convolution $|x*\varphi|$ of a time series $x(t)$ and a wavelet $\varphi(t)$ defines the time series energy near the center frequency of this wavelet as a function of time. A wavelet transform is the convolution of a time series with a filter bank with various center frequencies (Fig 1A left). The wavelets of a given bank $\varphi_\lambda(t)$ are dilated versions of a mother wavelet $\varphi_0(t)$ with a scaling factor λ such as $\varphi_\lambda(t) = \lambda\varphi_0(t\lambda)$. The frequency range of a wavelet transform is controlled by the number of octaves J, and the frequency resolution is given by the number of wavelets per octave Q. The total number of wavelets in a bank is $F = JQ$.

A wavelet transform defines a time-frequency representation of a signal called a *scalogram*, as illustrated from a SEIS record in Fig 1A. The evolution of modulating signals or longer trends in the envelopes cannot be captured with a single wavelet transform when several orders of magnitude exist between the time scales, as usually observed in seismology. On Earth, for instance, earthquakes often produce signals with sharp onsets and broad frequency contents. However, in the same frequency range, we can also observe non-volcanic tremor signals without clear onsets (e.g. Obara, 2002). Similar observations are made on Mars for the seismic noise recorded by SEIS: In addition, we observe both localized pressure drop signals and continuous wind-generated noise in equal frequency bands (Lognonné et al., 2020; Kenda et al., 2020; Charalambous et al., 2021). This motivates a design of a deep scattering network with three layers (Fig 1A). Each layer outputs scattering coefficients (see Fig 1A, right), the order corresponding with the layer index. The scattering coefficients from all orders define the set of features used later in our clustering procedure. The invariance properties of this network promote robust clustering. The dimension of one-dimensional data through the scattering network is summarized in Table 1. The time-pooling factor is adapted at each layer to allow for concatenating the scattering coefficients at all layers.

The 3 axis SEIS data are individually transformed and the scattering coefficients obtained from each component are concatenated to form a set of features for the three components within different time windows. The number of scattering coefficients obtained from a single time window can be significant depending on the number of wavelet filters and scattering orders. This full scattering representation is highly redundant since the input signals may share similar properties at different frequencies, so there is no need to keep the entire scattering representation. For this reason, we perform a dimension reduction of the scattering coefficients with a projection on the first few principal components (Fig 1B), corresponding to a low-dimensional representation (or latent space) where the clustering is applied.

2.3 Clustering with Gaussian Mixture Models

The overall clustering procedure is depicted in Fig 1A. Once transformed into a low-dimensional latent space, the different time windows of seismic data are clustered with a Gaussian Mixture Model (GMM). The different groups of time windows are ultimately interpreted as clusters of events. As in Seydoux et al. (2020), the mother wavelets at each

scattering layer are learned by minimizing the clustering loss of the GMM. Learning the wavelets is indicated by the back-propagation arrow in Fig 1B.

The learning procedure involves two steps. First, we define the value and derivative of the mother wavelet on K knots at each layer of the scattering network. The full wavelet is then interpolated with Hermite cubic splines. The number of knots is low to minimize the number of parameters to learn (for instance, with a wavelet defined on 5 knots, we need to learn 10 parameters; seven for both amplitude and derivative). A three-layer scattering network with wavelets defined on 5 knots involves 30 learnable parameters. In the second step, we learn the three mother wavelets that maximize the clustering quality. Following Seydoux et al. (2020), we use the ADAM stochastic gradient descent in order to incrementally converge towards an optimal solution, back-propagating the GMM clustering loss. In order to prevent trivial solutions from being learned (e.g., zero-valued wavelets), we include a partial reconstruction loss to preserve the input signal's energy across the network. For each layer, the reconstruction loss is the quadratic error between the input signal and the partially reconstructed signal (see Seydoux et al., 2020, for more formal details).

The deep scattering network can be seen as a particular, regularized Convolutional Neural Network (CNN), while the output is generated layerwise. In addition, the deep scattering network filters are reminiscent of physically meaningful signal processing as these involve multiple time and frequency analyses of the input data; this is illustrated in Table 1. This is an advantage over traditional CNNs which was demonstrated in Andén & Mallat (2014) and Oyallon et al. (2017).

2.4 Hyperparameters

The overall clustering strategy involves several hyperparameters that define the network architecture, control the time and frequency scales and temporal resolution of the analysis based on the frequency content of the tracked event, and the maximum number of clusters found by the procedure. We here define these parameters:

- **The number of scattering layers** L. Andén & Mallat (2014) suggest that two layers are sufficient for audio signals, especially with a broad frequency spectrum. In our case, we use 3 layers since the signals of interest span a narrow frequency

band, with the second and third layers designed to focus on the envelope oscillations at different frequencies (see Section 2.2).

- **The decimation factor**: The main idea of the deep scattering network is to capture the frequency content of the signals' envelope at different frequencies. For seismic data, we assume the envelopes vary smoothly with respect to time. We thus decimate the output of the different wavelet transforms at all layers by a given decimation factor. As a consequence, the temporal sampling of each layer reduces as depth increases (see Table 1).
- **The number of octaves** J_ℓ: determines the frequency range of the wavelet filter bank at layer ℓ, from $\omega_{\min} = \pi 2^{-J_\ell}$ to $\omega_{\max} = \pi$ (in radians). In the first layer, J_1 defines the frequencies analyzed in the seismic data. The parameters J_2 and J_3 control the ranges of time scales seen in the signal envelopes.
- **The number of wavelets per octave** Q_ℓ : controls the frequency resolution of each scalogram. Following Seydoux et al. (2020), we use a large Q in the first layer (dense representation) and a low Q in deeper layers (sparse representation) to maximize the separation between dissimilar events.
- **The number of wavelet knots** K: controls the number of points to interpolate the wavelets, and therefore the potential complexity in wavelet shape. Selecting more knots leads to a better description of the signal at reduced computational efficiency. To approximate standard mother wavelets such as the Gabor wavelet at affordable computation cost, we use K = 5 knots.
- **The latent space dimension**: controls the number of components to keep in the dimension reduction with Principal Component Analysis (PCA). There is a trade-off to consider between removing too much information (few principal components) and degrading the GMM clustering quality (too many principal components). Judging this trade-off, in the present study, we selected 6 components to perform the analysis.

3 Application to SEIS continous data

We focus on the continuous 20 samples per seconds (sps) VEL channels of the oblique VBB components U, V and W. The two top panels of Fig. 2 show one sol (184) of VBB U raw data and its spectrogram. Sols are Martian days (about 24 hours and 40 minutes) and are numbered since the landing date. A LMST hour is 1/24 of a sol.

As already described by Lognonné et al. (2020); Giardini et al. (2020); Stutzmann et al. (2021); Ceylan et al. (2021), SEIS signals contain highly repetitive patterns in both noise amplitude and frequency of events (that we define here as short duration bursts of energy) from one sol to another. Because of this sol-periodicity, we can expect to cover with a limited number of sols all patterns embedded in the noise, which will need only a few weeks for signal training. The first is from June, 3, 2019 to June, 11, 2019, coinciding with the start of continuous 20 sps data. We selected also three other weeks in 2019 (June 12 to 18, June 23 to 30 and July 7 to 14), in order to check that our unsupervised deep learning algorithm (see Section 2.2) can cluster the noise structure regardless of the duration and epoch of the time-period. As clustering results are similar for the four weeks, we show only the results for the first week.

In order to interpret the clustering results, we have also used the temperature data from SEIS and the temperature and pressure data from the Auxiliary Payload Sensors Suite (APSS) experiment Banfield et al. (2018). See further details in section "Data and Resources".

3.1 Data pre-processing and learning convergence

Minimal pre-processing was performed on the continuous data, limited to (i) a decimation by 2 due to available GPU memory limitations and (ii) a 0.001 Hz high-pass filtering, to remove the very long period thermal signal. All data are therefore expressed in Digital Unit (DU), which correspond to about 1.25 10^{-11} m/s at 1 Hz. Our various tests confirmed that the resulting 0.001-5 Hz 10 sps 3 axis continuous was sufficient for the clustering task.

Table 1 summarizes the choice of hyperparameters and dimension of the feature vectors used in our clustering approach. The continuous data was segmented in 100 s duration intervals viewed as samples without overlap due to processing limitation. Even if DSN has been able to track and cluster events close from the window's borders, future optimization can easily be made with overlapping.

The most frequent events in the data (like those generated by pressure drops or glitches) do not need many interpolation points for their reconstruction by the mother wavelets in each layer. As mentioned before, we set K to 5 and the latent space dimension to 6.

J_ℓ, Q_ℓ values and Nyquist frequencies, determining the bandwidth of each layer, are provided in Table 1.

Up to 9000 iterations (or epochs) were possible for the learning, but a stopping criterion after 2000 epochs was introduced, based on training's track and reconstruction losses and with awareness of the plateau phenomenon (Seydoux et al., 2020), found generally in the first 500 epochs. We tested our deep scattering network (DSN) with different depths and concluded that 3 layers were sufficient to extract information from noisy data and guarantee stability during learning. While a maximum of 15 clusters was allowed for the clustering, the clustering converged toward the smaller number of 9 clusters. This convergence to 9 clusters was found for different maxima tested (from 10 to 20) and was also found for training on either one week of data or only one sol.

3.2 Clusters and centroid for one sol

Figure 2 shows how the 885 100sec data samples cluster during sol 184, one of the sol of the week learning period. It provides the number of data samples per hour for each cluster as a function of the Local Mean Solar Time (LMST) at the InSight location. Cluster's occurrence frequency is described in figure 2. For example, cluster 0 is the most frequent cluster with 226 samples found, while cluster 8 is the least frequent one, with 24 samples. This already shows that all clusters are associated to specific LMST and are therefore thermally triggered or associated to specific temperature/pressure conditions. Clusters 0,1,2 occur during day time, clusters 4, 6, 7, 8 during early night and clusters 3 and 5 during late night. This will be confirmed by results for one week, presented later in the discussion and illustrated in the appendices.

These data samples are clusterized either due to similar events occurring in the 100 sec window or due to similar noise properties (e.g. level or color) in these windows. Before continuing the interpretation, we first briefly review the types of events already identified on SEIS data. These can be divided into two families:

- **Frequent events**: These appear every sol and are either associated with the Martian environment, the lander and/or the SEIS instrument. First examples are the pressure drops generating ground deformations. See Banerdt et al. (2020), Lognonné et al. (2020) and Kenda et al. (2020) for their signal on SEIS and Banfield et al. (2020) for the pressure signal on APSS. Spiga et al. (2021) and Lorenz et al. (2020)

catalogued them, based on the pressure signal shape. Other wind bursts examples appear through lander vibrations. See among other (Ceylan et al., 2021; Charalambous et al., 2021). Finally, due to thermoelastic stress release and also to pressure drops, glitches are very frequent on all SEIS records, with a visual repeatability sol by sol. See Lognonné et al. (2020) and Scholz et al. (2020) for more details. They generate micro-tilts, leading to high amplitude instrument responses in the raw data.

- **Rare events**: For our analysis, rare events are the seismic events (Giardini et al., 2020). With a rate of a few events per sol (Clinton et al., 2021), they are much less frequent than those listed above. In the framework of this paper, these will not be captured by clustering. Furthermore, for all the weeks analyzed, no correlation between reported P or S arrival times (as given by InSight Marsquake Service (2020)) and any cluster's event origin time was found. The frequency of event clusters during the seismic events was similar to the one found at the same LMST but for sols without events.

To better quantify common waveform similarities between samples of the same cluster, we extracted for each cluster their centroid waveform and compared them to the best similarity (BS) waveform. The later is by definition the closest to the covariance ellipsoid's center in the scattering manifold, distance corresponding in the machine learning vocabulary to the similarity coefficient. For a given cluster, the centroid waveform is the waveform stack of all events of the cluster and is obtained as follows. First all events from the cluster are aligned with the BS waveform and sorted with increasing correlation coefficient. See Figure 3 for cluster 6. Alignment is made by maximum correlation time-lag and correlation is computed in a 100 s window. The weighted stack is then obtained from the aligned waveforms as follows:

$$X(t) = \sum_{i=0}^{N} \omega_i x_i(t - \tau_i) \ ,$$

where ω_i is the correlation weight and τ_i is the correlation time-lag of the event i with respect to the reference.

For the 9 clusters, centroid waveforms are shown in Figure 4 while the data waveforms are shown in Appendix A (Figures A3 to A11 respectively). The BS waveforms for these 9 clusters are provided in Figure A12 of Appendix A. For each cluster, the cor-

relation and similarity values between the BS and centroid waveforms are shown on Figure 5 and support a classification in three families, listed A, B, C.

Clusters A (numbered 6-7-8) are characterized by both a high correlation and a high similarity between the BS waveform and the centroid. While having no significant similarity, the B type centroids (numbered 3,4,5) conserve a high correlation with the BS waveform for clusters 4 and 5. Correlation drops to about 0.5 for cluster 3. Clusters C are those numbered 0,1,2. They have a very low correlation but with a significant similarity for 1 and 2.

Both centroids and BS waveforms of families A and B are characterized by VBB glitches, as identified by Lognonné et al. (2020) and Scholz et al. (2020). They appear on these raw data as the instrument response to an acceleration step. The glitches are less clear for cluster 3 BS waveform and appear mostly on the corresponding centroid. The centroids and BS waveforms of family C are all occurring during windy activity, either during the day regime for clusters 1 and 2 with their larger spectral amplitudes or in the second part of the night, continuing to the morning for cluster 0. We will see later that these clusters are associated either to pressure drops or wind burst, generating in both cases SEIS signal.

The clustering is, however, not made only on the waveform similarities, but also on their spectral properties, including spectra color and ratio between high frequency and low frequency amplitudes. This explains why these families have several clusters and not only one and is illustrated by the spectra of the 9 centroid waveforms shown in figure 6 for the V component and in Appendix A (figure A13) for the associated BS spectra.

The large differences in the ratio between low-frequency and high-frequency amplitudes for family A and B confirm differences between the 5 clusters. For example, centroid's spectra of clusters 3, 4 and 7 are comparable above 1Hz but have growing amplitudes between 0.1-0.2Hz while the high frequency amplitudes and color of centroid's spectra 6, 8, and 5 are respectively red, white and blue. Likely, the clustering is also sensitive to the 1 Hz tick noise (and associated 2Hz-3Hz harmonics) which acts as an amplitude reference. While being an artifact related to the interference of the house keeping data inrush current on the VBB feedback analog signal, its amplitude is indeed stable over time (Ceylan et al., 2021). Another interesting feature is the 2.4Hz resonance

peak, proposed as a ground resonance by Giardini et al. (2020). It has a very comparable amplitude for the three low noise clusters (3,4,7), which confirms the stability of its amplitude. Clusters 3, 4-8 all occur during the night. But clusters 5 and 6 have a much larger noise level, covering the 2.4 Hz resonance, while cluster 8 has the highest background noise of both family A and B. For the family C, spectra are on the other hand much more comparable after scaling. The 1Hz tick noise allows however to understand that clusters 0, 2, 1 are associated to growing noise level, the tick noise being for example observed on both the BS waveform and the centroid for cluster 0 and absent for cluster 1. We will discuss this family later, in more detail, after having compared these clusters with pressure drops statistics.

Other VBB components provide similar results (Figures A1 for W and A2 for U) but with amplitude differences of the 1 Hz, 2 Hz, 3 Hz and 2.4 Hz peaks.

3.3 Clustering stability

The stability of the clustering is tested with training on different sols selected from the middle of Northern spring to the middle of Northern summer. Between 8 and 10 clusters are commonly identified. Four clusters (1,2,3,7) are stable over time, representing families A, B and C for clusters 7, 3 and 1-2 respectively. A similarity larger than 95% between events from different sols but from that same stable cluster is found. The centroid spectra are shown on Figure 7 for all these sols.

The two clusters with the lowest spectral amplitudes have clear 1 Hz (and overtones) tick noise peaks plus the 2.4 Hz resonance and correspond to clusters 7 and 3 from Figures 4 and 6. As already said, they are associated with glitches occurring during the early and late night, respectively, and therefore with decreasing cooling rate, which might explain the smaller glitch amplitude of cluster 3 as compared to 7, as illustrated by the almost 20 db differences in figure 6. The two other clusters are those with the largest spectral amplitudes, have large excitation levels for the lander resonances above 3 Hz and correspond to clusters 1 and 2 from Figures 4 and 6. These two clusters appear during the day or the second half of the night, respectively. We will later see that cluster 1 is associated with pressure drops, while cluster 2 is associated with bursts of energy generating ringing associated with the lander resonances. This ringing is also found when examining the spectrograms of individual events.

These clustering stabilities from sol to sol are likely related to both the waveform and spectra similarities, including for spectra resonances. The invariance properties of the deep scattering network contribute to these stabilities.

4 Comparison between SEIS glitch clusters and glitch catalog

Families A and B are characterized by powerful (for cluster 4-8) and weak (for cluster 3) glitches. Glitches from clusters 4 and 8 are dominating the signal in the time domain (Figure 2). During sol 184, they sum up to 364 events. These glitches are frequent enough to occur during quakes and perturb the recorded quakes signals (Lognonné et al., 2020).

Cataloging the glitches and possibly removing them was an early effort (Lognonné et al., 2020) and is detailed by Scholz et al. (2020). We compare here the detection timing of the DSN with those provided by the more classical glitch detection techniques. On sol 184 (June, 3, 2019), the number of glitches reported in these catalogs ranges from 50 to more than 200, depending on the detection algorithm and threshold parameters, and we use for comparison a catalog of 127 glitches obtained for a middle threshold value (see Supplementary material for the associated listing and further details in Scholz et al. (2020)). The histogram of the results is shown in Figure 15. The zero-centered distribution confirms the matching between the two approaches. In fact, DSN retrieves 117 glitches from the catalog out of 127 with a timing error smaller than 2 s, which corresponds to 92 % of the cataloged glitches and therefore 8% of false negative. When looking on the similarity coefficient, 170 of these events have a very low similarity coefficient, smaller than 10^{-8}, and can therefore be either false detection or weak detection. The total of glitches detected by DSN with high similarity is therefore 194 (152% of the cataloged glitches). These additional events are likely glitches with amplitude lower than the catalog threshold.

4.1 Cluster polarizations

Polarization provides additional information on the origin of clusters, and we determined the azimuth and dip for all events as follows. We first high-pass filter all components with a 0.1 Hz cutoff. We then normalized all components with the transfer function of the U component (a correction made by the ratio of the U transfer function with

the transfer function of the component) and then rotated the data to obtain the N, E, and Z components (based on SEED dataless information). The event's azimuth and dip are then computed using the Ppol software (Fontaine et al., 2009; Scholz, 2020). For all clusters except 1 and 3 we use a ±5s time window around the event center, as defined by the correlation with the centroid. For clusters 3 and 1 a window of ±40s and ±20s respectively is used.

Figure 10 shows the back azimuths and dips of all events from clusters 1, 3 and 8, while those of the other clusters are only discussed below. Cluster 0 and 1 have sub-vertical dip, as observed by Kenda et al. (2020) for pressure drops. Cluster 2 has a horizontal dip but with a relatively large azimuth scatter, even if some clustering toward North is observed with large amplitude. We retrieve here observations from Stutzmann et al. (2021); Charalambous et al. (2021) and an interpretation based on wind-induced lander noise. Cluster 8 is typical for SEIS glitches (like clusters 4 to 8). Its dip departure from horizontal is very small (as for cluster 7) and its azimuth points to the North (as for clusters 4,6 and 7) and seems related to longitudinal micro-tilts with respect to the tether. The not shown cluster 5 has on its side an azimuth close to orthogonal from the Load Shunt Assembly (LSA)/tether in line with their peak occurrence during the cooling of the early night (Figure 2), while those with smaller amplitude have still a sub-horizontal dip. Cluster 3 has more vertical component but a relatively stable azimuth toward the lander and correspond to either low amplitude glitches or internal SEIS glitches, known as source of vertical signal (Scholz et al., 2020).

5 Correlation of SEIS clusters with temperature and sol quasi periodicity

Both the dependency on LMST and the clustering stability over sols suggest that our clusters are driven by daily temperature variations. This is confirmed by Figure 8 which shows for five days, the number of events per hour together with the outside temperature, the scientific temperature and the VBB temperature. The latter two have a delay related to 3 hr and 5.5 hr time constant of the VBB enclosure and WTS (Lognonné et al., 2019). None of these temperature data were input of the learning.

We first discuss the correlation of occurrence rate with temperature starting from midnight (0:00 LMST). During the nighttime cooling and associated decrease of atmo-

spheric temperature, cluster 3 (green) is dominant, with a low noise level (Figure 6) and a clear 2.4 Hz resonance. Glitches from cluster 5 are also present in background, especially when noise levels are larger.

Cluster 0 (blue), with a much larger noise above 1Hz, hiding the 2.4 Hz resonance (Figure 6), increases in intensity when night winds rise up, and . This cluster replaces cluster 3 and becomes the most abundant in the early morning. Cluster 1 (orange) starts when the temperature increases after sunrise and reaches its maximum occurrence rate in the late morning. During the daytime's atmospheric activity this cluster dominates. The occurrence rate of cluster 2 (red) is increasing in the late morning and has a plateau between 12:00 and 17:00 LMST. Clusters 0, 2 and 1 have increasing background noise levels (Figure 6). This behavior is related to afternoon wind bursts, the signature of which is also found in the large variations in atmospheric temperature. Clusters 0, 1 have both long-period events and short-period events. They seem to be associated with the conjunction of pressure drops and wind burst. Cluster 2 is mostly a high-frequency event and is likely associated with wind bursts.

Thermal glitches, identified with clusters 3-8 are mostly occurring for 4-8 during the cooling phase of the late afternoon, reaching maximum activity between 18:00 and 20:00 LMST and a diffuse activity all the night. Cluster 3 glitches are on their side observed almost all the night.

For all clusters, the sol by sol repetition suggests that the clustering is able to capture the waveform and noise differences of these events, and that these are directly related to LMST and/or to a physical processes depending on LMST. Although the sequence is found every sol, differences in amplitude and in start/end times for each cluster are observed in sol to sol comparisons, as shown in Figure 8. Climatic variation will need further analysis but we can expect these to generate mostly a drift of the occurrence LMST time of the temperature correlated clusters.

6 Characterization of SEIS multi-glitches

Our approach detected another type of events in the data: these are glitches appearing in pairs, repeating with a stable time offset within the event window, and also repeating as the previous one every sol. We refer to these as doublet and, more generally, tuplet glitches.

To identify these, we simply increased the basic time window from 100 sec to 1200 sec. We now obtained 6 clusters. For a test made on 2 weeks of data in April 2019, the learning process converged after 8000 epochs and detected sequences of tuplet glitches with quasi-periodic recurrence times of 83 s, 208 s, 280 s, 295 s, 327 s and 374 s. We provide further details in Appendix B and Figure B1. For a 2-week period in June 2019 (from sol 183 to sol 197), the quasi-period recurrence times found are 91 s, 198 s, 208 s, 218 s, 280 s, 368 s and 385s. We provide further details in Appendix B and Figure B2. Although the recurrence times vary slightly, they concentrate in the ranges 80-90 s, 195-220 s, 280 s and 365-385 s. Figures 9 shows examples of glitches repeating with about 368 s delay, with 574 events found during a long sequence, from sol 184 to sol 198), and the aligned weighted stack of all these events. A mean rate of about 28 events per sol is therefore found for these events and the rms of the 368 s time offset is only 2.3 s. An interesting finding is that these signals are not present during some periods of the night, roughly between 1 LMST and 7 LMST. Further works, outside the scope of this paper, will be necessary to understand if they are instrument or lander generated.

Clearly, the occurrence of these glitches cannot be assumed as random and this might impact analysis assuming stochastic ambient noise. In this regard, the timing of mantle and core signals proposed by Deng & Levander (2020) from auto-correlation of the raw (and non-deglitched) SEIS data are coinciding with the 280s and 380s delays found in doublet clusters. An in depth analysis of the impact of glitches has been made by Kim et al. (2021), confirming that these signals must be handled with care for any geophysical interpretation. To our knowledge, the clustering analysis proposed here is at this time the only proposed method enabling the identification in the SEIS data of doublets and, generally speaking, of multi-glitches with non-stochastic timing. It furthermore allows us to find periods in the data, during which these signals disappear, and which might be more adequate for auto-correlation analysis.

7 Pressure drop clusters and catalog

We now analyze the correlations between SEIS micro-event clusters and pressure drops induced by atmospheric vortices, very frequent in Elysium Planitia (Banfield et al., 2020) and more generally the efficiency of clustering for pressure signals. We do it first with a clustering analysis of the pressure signal alone and then, compare the tim-

ing of pressure clusters and the SEIS clusters obtained in the previous sections with pressure drop catalogs (Lorenz et al., 2020; Spiga et al., 2021).

7.1 Cataloging pressure drops with DSN

For the first step, we use only 2 layers in the DSN structure and limit the principal component analysis to 3 components instead of 6. This focuses on the most frequent and clearest events. The 10 sps calibrated pressure data (Banfield et al., 2020b) were used. The training was made with pressure data starting on 2019-06-02 00:00:00 UTC and ending on 2019-06-11 00:00:00 UTC, covering sols 182 to 191.

We obtained 7 clusters, described in Appendix D and focus here on the three clusters clearly associated with pressure drops. Their stacks are shown on Figure 11 and these clusters differ by their frequency content and waveform shape. The less frequent events from cluster 2 have for example a more pronounced peak shape than those of cluster 0 and 1.

7.2 Pressure drop catalog correlation with the pressure clusters

To confirm the link with pressure drops, we use the published pressure drop catalog. It reports 278 pressure drops larger than -0.3 Pa during the learning period. For each event of the three clusters, we determine first its time through cross-correlation with the cluster centroid waveform and compute then the time difference with the closest cataloged pressure drop. Events with a time difference larger than the learning window (100s) are rejected(about 8%). The learning detected 341 events for cluster 0, 566 events for cluster 1 and 24 events for cluster 2, respectively. Similarity coefficients were larger than 0.00018 for cluster 0, 5.310^{-7} for cluster 1 and 0.0019 for cluster 2, respectively. 111.9% (311 learned events out of 278 in the pressure drop catalog) of the reported dust devils are within this 100 sec window, and 92% have furthermore a time difference of less than 20s. DSN can therefore catalog the pressure drops directly from pressure data, and in addition improve the detection of smaller and not yet reported ones. For these 2 clusters we detected 3.34 times more events than those found manually, with pressure amplitudes of -0.015 Pa for cluster 0, -0.017 Pa for cluster 1 and -0.2 Pa for cluster 2, respectively.

Figure 12 shows the occurrence time difference between the DSN detected pressure drop and those of the catalog. Most of the events timing are within ± 5 sec from those

of the catalog. Note also the secondary peaks, mostly 25 sec prior, which is likely related to double pressure drops structure.

Figure 13 summarizes the results with a frequency-amplitude log-log cumulative histogram. This shows that the power -2 slope proposed by Lorenz et al. (2021); Spiga et al. (2021) can be extended to lower amplitudes and at least down to 0.2 Pa. This doubles the number of pressure drops. The cluster 2, with a sharp pressure drop, seems more sensitive to noise and is found only for the largest pressure drop while the cluster 0 might complete, for low amplitude, the cluster 1. Machine learning is therefore efficient and likely better at detecting and classifying pressure drops than previous studies made with InSight data.

7.3 VBB clusters correlation with the pressure clusters

Let us now compare the occurrence time of the seismic VBB clusters and those of the published dust devils catalog, to identify VBB events related to pressure drops. Cluster numbers are those from section 4-6.

Let us first focus on pressure drops found with a time delay within ± 100 sec to a cluster event. For a cluster with a rate of N event per sol, a fraction of these might be coincident just by chance. In such a random process, the probability to get n pressure drops in the N windows of ΔT=200 sec is $p(n) = a_0^n C(N,n)$ where $C(N,n)$ is the binomial coefficient of n-combinations over N and $a_0 = \frac{\Delta T}{sol}$, where *sol* is the duration of one sol. This provides the 1σ threshold for all cluster, respectively equal to n=13,13,3,8,3,6,3,2,2 for clusters 0 to 8. These numbers were all computed for the reference period detailed in Appendix A, where the list of all clusters can be found.

Only 5 clusters are found above the 1σ threshold, with associated histograms in Figure 14: clusters 0, 1, 2, 4 and 8, with a number of pressure drops respectively 14x, 7x, 6x, 1.5x and 8.5x those of the 1σ thresholds. For the 201 pressure drops reported in the test period from June 3 to June 10, 2019, 90% (respectively 50%) of these pressure drops can be associated with an event of cluster 0 (respectively 1).

With a closer look at Figure 14, we find pressure drops within ±25s for cluster 0 and ±40s for cluster 1. In addition, we observed on the centroid waveforms (figure 4), long period oscillations, 25s before the event's center for cluster 0 and 40s before for cluster 1. VBB events are therefore detected in advance of the drop in pressure data. The

glitch clusters 4 and 8 are also correlated with pressure drops. Their dip is close to horizontal, suggesting generation by the pressure drop of a micro-tilt on the instrument, in contrary to clusters 0 and 1 for which the signal has a significant vertical component. Finally, some of the events of cluster 2, related to wind bursts, are also associated with pressure drop. They account only for about 10% of the pressure drops and are likely related to the high winds observed during the pressure drops events.

Conclusion

The Deep Scattering Network DSN method has proven to be powerful and effective when applied to the Martian dataset gathered by the InSight mission. It has successfully classified the dynamics of the noise in an automatic and unsupervised way. DSN is capable of extracting multiple features in a large dimensional space, to which the noise is mapped. This allows us to better understand and identify the properties in each time window of SEIS and pressure data. Naturally, the DSN approach can be generalized to other time series. With the multiple wavelets cascade and activation functions, patterns that cannot be easily identified are retrieved.

As a result, we detected multiple environmental Martian events like glitches, pressure drops, and wind bursts with efficiency and sensitivity comparable with the published catalogs but in a full unsupervised way. More importantly, the DSN was able to discover and characterize, for the first time, tuplets of glitches, whose stable separation in time must be integrated in future auto-correlation analysis to ensure that these quasi-periodic events are not misinterpreted in terms of deep interior seismic phases. DSN appears therefore as a powerful tool for studying the non-stochasticity of seismic noise and finding noise structures both in terms of waveform and spectra. When implemented on continous data, this will allow possible misinterpretation between seismic phases and micro-seismic noise bursts, especially for low signal-to-noise events.

This analysis also shows that unsupervised deep learning efficiently identifies clusters of micro-events in seismic data. If used in parallel with more classical seismic detection algorithms, this could prevent detection saturation and select noise samples for future planetary or Earth's ocean bottom geophysical observatories unable to fully transmit their data. In this regard, DSN can not only enhance the robotic system performance but also increase science return.

Data and Resources

SEIS data used are available in SEED format (InSIght Mars SEIS Service, 2019a) or PDS4 format (InSIght Mars SEIS Service, 2019b) at the respective doi's: 10.18715/SEIS.INSIGHT.XB 2016 and 10.17189/1517570. Pressure and atmospheric data are available at NASA PDS at the respectives doi's: 10.17189/1518939 and 10.17189/1518950. Namely, we used in addition to seismic data the VBB sensor's temperatures (03.VKU, 03.VKV, 03.VKW), the Leveling System (LVL) temperature (VKI), and for APSS, the atmospheric temperature (VKO) and pressure (03.BDO). Catalogs are available for MQS event in InSight Marsquake Service (2020), for pressure drops in Spiga et al. (2021) and for glitches in Scholz et al. (2020). The deep scattering network clustering algorithm used in this study was downloaded from its original repository at https://github.com/leonard-seydoux/scatnet. This paper is accompanied by a supplementary material divided into two sections.

The first part corresponds to the learned pressure drops data (3 files) and documents all events of the 3 pressure drop clusters shown in the paper. In each file, columns provide the event index, the UTC time, the similarity coefficient, the correlation coefficient, the amplitude and finally the amplitude of the event in Pa.

The second section describes the VBB cluster's data and documents all events of the 9 VBB clusters shown in the paper. In each file, columns provide the event index, the UTC time, the similarity coefficient, the correlation coefficient and the amplitude of respectively U, V and W channels. All correlation coefficients are those with the event having the highest similarity coefficient, as explained in the paper

Acknowledgments

We acknowledge NASA, CNES, their partner agencies and Institutions (UKSA, SSO, DLR, JPL, IPGP-CNRS, ETHZ, IC, MPS-MPG) and the flight operations team at JPL, SISMOC, MSDS, IRIS-DMC and PDS for providing SEED SEIS data. SB acknowledges CNES and the ED560 STEP'UP for her PhD support. French authors are supported by ANR MAGIS (ANR-19-CE31-0008-08) and by CNES for SEIS science support. MVdH was supported by U.S. Department of Energy, Office of Science, Office of Basic Energy Sciences, Chemical Sciences, Geosciences and Biosciences Division under grant number DE-SC0020345 and the Simons Foundation under the MATH + X program. We thank the editor, V.Tsai and the two anonymous reviewers for their fruitful reviews which have

improved greatly the manuscript, as well as R.Weber for her review and reading. This is the InSight contribution number 83 and IPGP contribution number XXX.

References

Andén, J., & Mallat, S. (2014). Deep scattering spectrum. *IEEE Transactions on Signal Processing*, ***62***(16), 4114-4128.

Banerdt, W. B., Smrekar, S. E., Banfield, D., Giardini, D., Golombek, M., Johnson, C. L., Lognonné, P., Spiga, A., Spohn, T., Perrin, C., Stähler, S. C., Antonangeli, D., Asmar, S., Beghein, C., Bowles, N., Bozdag, E., Chi, P., Christensen, U., Clinton, J., Collins, G. S., Daubar, I., Dehant, V., Drilleau, M., Fillingim, M., Folkner, W., Garcia, R. F., Garvin, J., Grant, J., Grott, M., Grygorczuk, J., Hudson, T., Irving, J. C. E., Kargl, G., Kawamura, T., Kedar, S., King, S., Knapmeyer-Endrun, B., Knapmeyer, M., Lemmon, M., Lorenz, R., Maki, J. N., Margerin, L., McLennan, S. M., Michaut, C., Mimoun, D., Mittelholz, A., Mocquet, A., Morgan, P., Mueller, N. T., Murdoch, N., Nagihara, S., Newman, C., Nimmo, F., Panning, M., Pike, W. T., Plesa, A.-C., Rodriguez, S., Rodriguez-Manfredi, J. A., Russell, C. T., Schmerr, N., Siegler, M., Stanley, S., Stutzmann, E., Teanby, N., Tromp, J., van Driel, M., Warner, N., Weber, R., & Wieczorek, M. (2020). Initial results from the InSight mission on mars. *Nature Geoscience*, ***13***(3), 183–189.

Banfield, D., , Rodriguez-Manfredi, J. A., Russell, C. T., Rowe, K. M., Leneman, D., Lai, H. R., Cruce, P. R., Means, J. D., Johnson, C. L., Mittelholz, A., Joy, S. P., Chi, P. J., Mikellides, I. G., Carpenter, S., Navarro, S., Sebastian, E., Gomez-Elvira, J., Torres, J., Mora, L., Peinado, V., Lepinette, A., Hurst, K., Lognonné, P., Smrekar, S. E., & Banerdt, W. B. (2018, December). InSight auxiliary payload sensor suite (APSS). *Space Science Reviews*, ***215***(1).

Banfield, D., Spiga, A., Newman, C., Forget, F., Lemmon, M., Lorenz, R., Murdoch, N., Viudez-Moreiras, D., Pla-Garcia, J., Garcia, R. F., Lognonné, P., Özgür Karatekin, Perrin, C., Martire, L., Teanby, N., Hove, B. V., Maki, J. N., Kenda, B., Mueller, N. T., Rodriguez, S., Kawamura, T., McClean, J. B., Stott, A. E., Charalambous, C., Millour, E., Johnson, C. L., Mittelholz, A., Määttänen, A., Lewis, S. R., Clinton, J., Stähler, S. C., Ceylan, S., Giardini, D., Warren, T., Pike, W. T., Daubar, I., Golombek, M., Rolland, L., Widmer-Schnidrig, R., Mimoun, D., Beucler, É., Jacob, A., Lucas, A., Baker, M., Ansan, V., Hurst, K., Mora-

Sotomayor, L., Navarro, S., Torres, J., Lepinette, A., Molina, A., Marin-Jimenez, M., Gomez-Elvira, J., Peinado, V., Rodriguez-Manfredi, J.-A., Carcich, B. T., Sackett, S., Russell, C. T., Spohn, T., Smrekar, S. E., & Banerdt, W. B. (2020). The atmosphere of mars as observed by InSight. *Nature Geoscience*, ***13***(3), 190–198.

Banfield, D., Spiga, A., Newman, C., Forget, F., Lemmon, M., Lorenz, R., Murdoch, N., Viudez-Moreiras, D., Pla-Garcia, J., Garcia, R. F., Lognonné, P., Özgür Karatekin, Perrin, C., Martire, L., Teanby, N., Hove, B. V., Maki, J. N., Kenda, B., Mueller, N. T., Rodriguez, S., Kawamura, T., McClean, J. B., Stott, A. E., Charalambous, C., Millour, E., Johnson, C. L., Mittelholz, A., Määttänen, A., Lewis, S. R., Clinton, J., Stähler, S. C., Ceylan, S., Giardini, D., Warren, T., Pike, W. T., Daubar, I., Golombek, M., Rolland, L., Widmer-Schnidrig, R., Mimoun, D., Beucler, É., Jacob, A., Lucas, A., Baker, M., Ansan, V., Hurst, K., Mora-Sotomayor, L., Navarro, S., Torres, J., Lepinette, A., Molina, A., Marin-Jimenez, M., Gomez-Elvira, J., Peinado, V., Rodriguez-Manfredi, J.-A., Carcich, B. T., Sackett, S., Russell, C. T., Spohn, T., Smrekar, S. E., & Banerdt, W. B. (2020b). *Insight apss ps data product bundle.* Retrieved from `urn:nasa:pds:insight_ps` doi: 10.17189/1518939

Bergen, K. J., & Beroza, G. C. (2018). Earthquake fingerprints: Extracting waveform features for similarity-based earthquake detection. *Pure and Applied Geophysics*, ***176***(3), 1037–1059.

Bruna, J., & Mallat, S. (2013). Invariant scattering convolution networks. *IEEE Transactions on Pattern Analysis and Machine Intelligence*, ***35***(8), 1872–1886.

Ceylan, S., Clinton, J. F., Giardini, D., Böse, M., Charalambous, C., van Driel, M., Horleston, A., Kawamura, T., Khan, A., Orhand-Mainsant, G., Scholz, J.-R., Stähler, S. C., Euchner, F., Banerdt, W. B., Lognonné, P., Banfield, D., Beucler, E., Garcia, R. F., Kedar, S., Panning, M. P., Pike, W. T., Smrekar, S. E., Spiga, A., Dahmen, N. L., Hurst, K., Stott, A. E., Lorenz, R. D., Schimmel, M., Stutzmann, E., ten Pierick, J., Conejero, V., Pardo, C., & Perrin, C. (2021). Companion guide to the marsquake catalog from insight, sols 0–478: Data content and non-seismic events. *Physics of the Earth and Planetary Interiors*, ***310***, 106597.

Charalambous, C., Stott, A. E., Pike, T., McClean, J., Warren, T., Spiga, A., Banfield, D., Garcia, R. F., Clinton, J., Stähler, S. C., & et al. (2021). A comodula-

tion analysis of atmospheric energy injection into the ground motion at insight, mars. *Journal of Geophysical Research: Planets*, ***126***, e2020JE006538.

Clinton, J., Ceylan, S., van Driel, M., Giardini, D., Stähler, S. C., Böse, M., Charalambous, C., Dahmen, N. L., Horleston, A., Kawamura, T., Khan, A., Orhand-Mainsant, G., Scholz, J.-R., Euchner, F., Banerdt, W. B., Lognonné, P., Banfield, D., Beucler, E., Garcia, R. F., Kedar, S., Panning, M. P., Perrin, C., Pike, W. T., Smrekar, S. E., Spiga, A., & Stott, A. E. (2021). The marsquake catalogue from insight, sols 0–478. *Physics of the Earth and Planetary Interiors*, ***310***, 106595.

Clinton, J., Giardini, D., Böse, M., Ceylan, S., Van Driel, M., Euchner, F., Garcia, R. F., Kedar, S., Khan, A., Stähler, S. C., Banerdt, B., Lognonne, P., Beucler, E., Daubar, I., Drilleau, M., Golombek, M., Kawamura, T., Knapmeyer, M., Knapmeyer-Endrun, B., Mimoun, D., Mocquet, A., Panning, M., Perrin, C., & Teanby, N. A. (2018). The Marsquake Service: Securing Daily Analysis of SEIS Data and Building the Martian Seismicity Catalogue for InSight. *Space Science Reviews*, ***214***(133), 1-33. Retrieved from `https://hal.archives-ouvertes.fr/hal-01991048`

Deng, S., & Levander, A. (2020). Autocorrelation reflectivity of mars. *Geophysical Research Letters*, ***47***(16), e2020GL089630.

Falcin, A., Métaxian, J.-P., Mars, J., Éléonore Stutzmann, Komorowski, J.-C., Moretti, R., Malfante, M., Beauducel, F., Saurel, J.-M., Dessert, C., Burtin, A., Ucciani, G., de Chabalier, J.-B., & Lemarchand, A. (2021). A machine-learning approach for automatic classification of volcanic seismicity at la soufrière volcano, guadeloupe. *Journal of Volcanology and Geothermal Research*, ***411***, 107151.

Fontaine, F. R. R., Barruol, G., Kennett, B. L. N., Bokelmann, G. H. R., & Reymond, D. R. (2009). Upper mantle anisotropy beneath Australia and Tahiti from P wave polarization: Implications for real-time earthquake location. *Journal of Geophysical Research : Solid Earth*, ***114***(B3), B03306.

Garcia, R. F., Kenda, B., Kawamura, T., Spiga, A., Murdoch, N., Lognonné, P. H., Widmer-Schnidrig, R., Compaire, N., Orhand-Mainsant, G., Banfield, D., & Banerdt, W. B. (2020). Pressure effects on the seis-insight instrument, improvement of seismic records, and characterization of long period atmospheric waves from ground displacements. *Journal of Geophysical Research: Planets*, ***125***(7), e2019JE006278.

Géron, A. (2019). *Hands-on machine learning with scikit-learn, keras, and tensorflow: Concepts, tools, and techniques to build intelligent systems.* O'Reilly Media, Sebastopol.

Giardini, D., Lognonné, P., Banerdt, W. B., Pike, W. T., Christensen, U., Ceylan, S., Clinton, J. F., van Driel, M., Stähler, S. C., Böse, M., et al. (2020). The seismicity of mars. *Nature Geoscience*, ***13***(3), 205–212.

Goodfellow, I., Bengio, Y., & Courville, A. (2016). *Deep learning.* MIT Press, Boston.

Hibert, C., Michéa, D., Provost, F., Malet, J.-P., & Geertsema, M. (2019). Exploration of continuous seismic recordings with a machine learning approach to document 20 yr of landslide activity in alaska. *Geophysical Journal International*, ***219***(2), 1138–1147.

InSight Mars SEIS Data Service. (2019). *Seis raw data, insight mission.* IPGP, JPL, CNES, ETHZ, ICL, MPS, ISAE-Supaero, LPG, MFSC. Retrieved from `http://datacenter.ipgp.fr/networks/detail/XB_2016/` doi: 10.18715/seis.insight.xb2016

InSight Marsquake Service. (2020). *Mars seismic catalogue, insight mission; v1 2/1/2020.* ETHZ, IPGP, JPL, ICL, ISAE-Supaero, MPS, Univ. Bristol. Retrieved from `http://www.insight.ethz.ch/seismicity/catalog/v1/` doi: 10.12686/A6

Jia, Y., & Ma, J. (2017). What can machine learning do for seismic data processing? an interpolation application. *GEOPHYSICS*, ***82***(3), V163–V177.

Jordan, M. I., & Mitchell, T. M. (2015). Machine learning: Trends, perspectives, and prospects. *Science*, ***349***(6245), 255–260.

Kenda, B., Drilleau, M., Garcia, R. F., Kawamura, T., Murdoch, N., Compaire, N., Lognonné, P., Spiga, A., Widmer-Schnidrig, R., Delage, P., Ansan, V., Vrettos, C., Rodriguez, S., Banerdt, W. B., Banfield, D., Antonangeli, D., Christensen, U., Mimoun, D., Mocquet, A., & Spohn, T. (2020). Subsurface structure at the insight landing site from compliance measurements by seismic and meteorological experiments. *Journal of Geophysical Research: Planets*, ***125***(6), e2020JE006387.

Kim, D., Davis, P., Leki, V., Maguire, R., Compaire, N., Schimmel, M., Stutzmann, E., Irving, J., Lognonné, P., Scholz, J.-R., Clinton, J., Zenhäusern, G., Dahmen, N., S.Deng, Levander, A., Panning, M., Garcia, R. F., Giardini, D., Hurst, K.,

KnapmeyerEndrun, B., Nimmo, F., Pike, W. T., Pou, L., Schmerr, N., Stähler, S. C., Tauzin, B., R.Widmer-Schnidrig, & Banerdt, W. B. (2021). Potential pitfalls in the analysis and structural interpretation of seismic data from the mars insight mission. *Bulletin of the Seismological Society of America*, .

Kong, Q., Trugman, D. T., Ross, Z. E., Bianco, M. J., Meade, B. J., & Gerstoft, P. (2018). Machine learning in seismology: Turning data into insights. *Seismological Research Letters*, ***90***(1), 3–14.

Lognonné, P., Banerdt, W. B., Giardini, D., Pike, W. T., Christensen, U., Laudet, P., de Raucourt, S., Zweifel, P., Calcutt, S., Bierwirth, M., Hurst, K. J., Ijpelaan, F., Umland, J. W., Llorca-Cejudo, R., Larson, S. A., Garcia, R. F., Kedar, S., Knapmeyer-Endrun, B., Mimoun, D., Mocquet, A., Panning, M. P., Weber, R. C., Sylvestre-Baron, A., Pont, G., Verdier, N., Kerjean, L., Facto, L. J., Gharakanian, V., Feldman, J. E., Hoffman, T. L., Klein, D. B., Klein, K., Onufer, N. P., Paredes-Garcia, J., Petkov, M. P., Willis, J. R., Smrekar, S. E., Drilleau, M., Gabsi, T., Nebut, T., Robert, O., Tillier, S., Moreau, C., Parise, M., Aveni, G., Ben Charef, S., Bennour, Y., Camus, T., Dandonneau, P. A., Desfoux, C., Lecomte, B., Pot, O., Revuz, P., Mance, D., tenPierick, J., Bowles, N. E., Charalambous, C., Delahunty, A. K., Hurley, J., Irshad, R., Liu, H., Mukherjee, A. G., Standley, I. M., Stott, A. E., Temple, J., Warren, T., Eberhardt, M., Kramer, A., Kühne, W., Miettinen, E.-P., Monecke, M., Aicardi, C., André, M., Baroukh, J., Borrien, A., Bouisset, A., Boutte, P., Brethomé, K., Brysbaert, C., Carlier, T., Deleuze, M., Desmarres, J. M., Dilhan, D., Doucet, C., Faye, D., Faye-Refalo, N., Gonzalez, R., Imbert, C., Larigauderie, C., Locatelli, E., Luno, L., Meyer, J.-R., Mialhe, F., Mouret, J. M., Nonon, M., Pahn, Y., Paillet, A., Pasquier, P., Perez, G., Perez, R., Perrin, L., Pouilloux, B., Rosak, A., Savin de Larclause, I., Sicre, J., Sodki, M., Toulemont, N., Vella, B., Yana, C., Alibay, F., Avalos, O. M., Balzer, M. A., Bhandari, P., Blanco, E., Bone, B. D., Bousman, J. C., Bruneau, P., Calef, F. J., Calvet, R. J., D'Agostino, S. A., de los Santos, G., Deen, R. G., Denise, R. W., Ervin, J., Ferraro, N. W., Gengl, H. E., Grinblat, F., Hernandez, D., Hetzel, M., Johnson, M. E., Khachikyan, L., Lin, J. Y., Madzunkov, S. M., Marshall, S. L., Mikellides, I. G., Miller, E. A., Raff, W., Singer, J. E., Sunday, C. M., Villalvazo, J. F., Wallace, M. C., Banfield, D., Rodriguez-Manfredi, J. A., Russell, C. T., Trebi-Ollennu, A., Maki, J. N., Beucler, E., Böse, M., Bonjour,

C., Berenguer, J. L., Ceylan, S., Clinton, J., Conejero, V., Daubar, I., Dehant, V., Delage, P., Euchner, F., Estève, I., Fayon, L., Ferraioli, L., Johnson, C. L., Gagnepain-Beyneix, J., Golombek, M., Khan, A., Kawamura, T., Kenda, B., Labrot, P., Murdoch, N., Pardo, C., Perrin, C., Pou, L., Sauron, A., Savoie, D., Stähler, S., Stutzmann, E., Teanby, N. A., Tromp, J., van Driel, M., Wieczorek, M., Widmer-Schnidrig, R., & Wookey, J. (2019). SEIS: Insight's Seismic Experiment for Internal Structure of Mars. *Space Science Reviews*, ***215***(1), 12.

Lognonné, P., Banerdt, W. B., Pike, W. T., Giardini, D., Christensen, U., Garcia, R. F., Kawamura, T., Kedar, S., Knapmeyer-Endrun, B., Margerin, L., Nimmo, F., Panning, M., Tauzin, B., Scholz, J.-R., Antonangeli, D., Barkaoui, S., Beucler, E., Bissig, F., Brinkman, N., Calvet, M., Ceylan, S., Charalambous, C., Davis, P., van Driel, M., Drilleau, M., Fayon, L., Joshi, R., Kenda, B., Khan, A., Knapmeyer, M., Lekic, V., McClean, J., Mimoun, D., Murdoch, N., Pan, L., Perrin, C., Pinot, B., Pou, L., Menina, S., Rodriguez, S., Schmelzbach, C., Schmerr, N., Sollberger, D., Spiga, A., Stähler, S., Stott, A., Stutzmann, E., Tharimena, S., Widmer-Schnidrig, R., Andersson, F., Ansan, V., Beghein, C., Böse, M., Bozdag, E., Clinton, J., Daubar, I., Delage, P., Fuji, N., Golombek, M., Grott, M., Horleston, A., Hurst, K., Irving, J., Jacob, A., Knollenberg, J., Krasner, S., Krause, C., Lorenz, R., Michaut, C., Myhill, R., Nissen-Meyer, T., ten Pierick, J., Plesa, A.-C., Quantin-Nataf, C., Robertsson, J., Rochas, L., Schimmel, M., Smrekar, S., Spohn, T., Teanby, N., Tromp, J., Vallade, J., Verdier, N., Vrettos, C., Weber, R., Banfield, D., Barrett, E., Bierwirth, M., Calcutt, S., Compaire, N., Johnson, C., Mance, D., Euchner, F., Kerjean, L., Mainsant, G., Mocquet, A., Manfredi, J. A. R., Pont, G., Laudet, P., Nebut, T., de Raucourt, S., Robert, O., Russell, C. T., Sylvestre-Baron, A., Tillier, S., Warren, T., Wieczorek, M., Yana, C., & Zweifel, P. (2020). Constraints on the shallow elastic and anelastic structure of mars from InSight seismic data. *Nature Geoscience*, ***13***(3), 213–220.

Lorenz, R. D., Lemmon, M. T., Maki, J., Banfield, D., Spiga, A., Charalambous, C., Barrett, E., Herman, J. A., White, B. T., Pasco, S., & Banerdt, W. B. (2020). Scientific observations with the insight solar arrays: Dust, clouds, and eclipses on mars. *Earth and Space Science*, ***7***(5), e2019EA000992.

Lorenz, R. D., Spiga, A., Lognonné, P., Plasman, M., Newman, C. E., & Charalambous, C. (2021). The whirlwinds of elysium: A catalog and meteorological

characteristics of "dust devil" vortices observed by InSight on mars. *Icarus*, ***355***, 114119.

Malfante, M., Mura, M. D., Metaxian, J.-P., Mars, J. I., Macedo, O., & Inza, A. (2018). Machine learning for volcano-seismic signals: Challenges and perspectives. *IEEE Signal Processing Magazine*, ***35***(2), 20–30.

Mora, L. (2019). *Apss ps data.* Atmospheres Node. Retrieved from `https://pds.jpl.nasa.gov/ds-view/pds/viewBundle.jsp?identifier=urn:nasa:pds:insight_ps&version=3.0` doi: 10.17189/1518939

Obara, K. (2002). Nonvolcanic deep tremor associated with subduction in southwest japan. *Science*, ***296***(5573), 1679–1681.

Oyallon, E., Belilovsky, E., & Zagoruyko, S. (2017, Oct). Scaling the scattering transform: Deep hybrid networks. In *Proceedings of the ieee international conference on computer vision (iccv).*

Peterson, J. (1993). *Observations and modeling of seismic background noise.* Open-File Report 93-322, U.S. Geological Survey.

Priyadarshini, I., & Puri, V. (2021, July). Mars weather data analysis using machine learning techniques. *Earth Science Informatics*, . Retrieved from `https://doi.org/10.1007/s12145-021-00643-0` doi: 10.1007/s12145-021-00643-0

Schimmel, M., Stutzmann, E., Lognonné, P., Compaire, N., Davis, P., Drilleau, M., Garcia, R., Kim, D., Knapmeyer-Endrun, B., Lekic, V., Margerin, L., Panning, M., Schmerr, N., Scholz, J. R., Spiga, A., Tauzin, B., & Banerdt, B. (2021, June). Seismic noise autocorrelations on mars. *Earth and Space Science*, ***8***(6). Retrieved from `https://doi.org/10.1029/2021ea001755` doi: 10.1029/2021ea001755

Scholz, J.-R. (2020, September). Ppol. Python code, `https://ppol.readthedocs.io/en/latest/`.

Scholz, J.-R., Widmer-Schnidrig, R., Davis, P., Lognonné, P., Pinot, B., Garcia, R. F., Hurst, K., Pou, L., Nimmo, F., Barkaoui, S., de Raucourt, S., Knapmeyer-Endrun, B., Knapmeyer, M., Orhand-Mainsant, G., Compaire, N., Cuvier, A., Beucler, , Bonnin, M., Joshi, R., Sainton, G., Stutzmann, E., Schimmel, M., Horleston, A., Böse, M., Ceylan, S., Clinton, J., van Driel, M., Kawamura, T., Khan, A., Stähler, S. C., Giardini, D., Charalambous, C., Stott, A. E., Pike, W. T., Christensen, U. R., & Banerdt, W. B. (2020). Detection, analysis, and removal of glitches from insight's seismic data from mars. *Earth and Space Science*, ***7***(11),

e2020EA001317.

Seydoux, L., Balestriero, R., Poli, P., de Hoop, M., Campillo, M., & Baraniuk, R. (2020). Clustering earthquake signals and background noises in continuous seismic data with unsupervised deep learning. *Nature Communications*, ***11***(1), 3972.

Spiga, A., Murdoch, N., Lorenz, R., Forget, F., Newman, C., Rodriguez, S., Pla-Garcia, J., Moreiras, D. V., Banfield, D., Perrin, C., Mueller, N. T., Lemmon, M., Millour, E., & Banerdt, W. B. (2021). A study of daytime convective vortices and turbulence in the martian planetary boundary layer based on half-a-year of insight atmospheric measurements and large-eddy simulations. *Journal of Geophysical Research: Planets*, ***126***(1), e2020JE006511.

Stutzmann, E., Schimmel, M., Lognonné, P., Horleston, A., Ceylan, S., van Driel, M., Stahler, S., Banerdt, B., Calvet, M., Charalambous, C., Clinton, J., Drilleau, M., Fayon, L., Garcia, R. F., Giardini, D., Hurst, K., Jacob, A., Kawamura, T., Kenda, B., Margerin, L., Murdoch, N., Panning, M., Pike, T., Scholz, J.-R., & Spiga, A. (2021). The polarization of ambient noise on mars. *Journal of Geophysical Research: Planets*, ***126***(1), e2020JE006545.

Authors mailing list

- Salma Barkaoui: barkaoui@ipgp.fr, Université de Paris, Institut de physique du globe de Paris, CNRS, F-75005 Paris, France
- Philippe Lognonné: lognonne@ipgp.fr, Université de Paris, Institut de physique du globe de Paris, CNRS, F-75005 Paris, France
- Taichi Kawamura: kawamura@ipgp.fr, Université de Paris, Institut de physique du globe de Paris, CNRS, F-75005 Paris, France
- Éléonore Stutzmann: stute@ipgp.fr, Université de Paris, Institut de physique du globe de Paris, CNRS, F-75005 Paris, France
- Léonard Seydoux: leonard.seydoux@gmail.com, Institut des sciences de la Terre, Université Grenoble-Alpes, UMR CNRS 5375, France
- Maarten De Hoop: mvd2@rice.edu, Rice University 2035 Duncan Hall, Houston, TX, USA.
- Randall Balestriero: randallbalestriero@gmail.com, Rice University 2035 Duncan Hall, Houston, TX, USA.

- John-Robert Scholz: scholz@mps.mpg.de, Max Planck Institute for Solar System Research, Justus-von-Liebig-Weg 3, 37077 Göttingen, Germany
- Grégory Sainton: sainton@ipgp.fr, Université de Paris, Institut de physique du globe de Paris, CNRS, F-75005 Paris, France
- Savas Ceylan: savas.ceylan@erdw.ethz.ch, Institute of Geophysics, ETH Zurich, Sonneggstr. 5, 8092 Zurich, Switzerland
- John Clinton:jclinton@sed.ethz.ch, Swiss Seismological Service (SED), ETH Zurich, Sonneggstr. 5, 8092 Zurich, Switzerland
- Aymeric Spiga: aymeric.spiga@sorbonne-universite.fr, Laboratoire de Météorologie Dynamique/IPSL, Sorbonne Université, CNRS, Ecole Normale Supérieure, PSL Research University, Ecole Polytechnique, 75005 Paris, France
- Rudolf Widmer-Schnidrig: widmer@gis.uni-stuttgart.de, Black Forest Observatory, Stuttgart University, Heubach 206, D-77709 Wolfach, Germany
- Francesco Civilini: francesco.civilini@nasa.gov, NASA's Marshall Space Flight Center, 320 Sparkman Dr. Huntsville AL 35805, Alabama
- W.Bruce Banerdt: william.b.banerdt@jpl.nasa.gov, Jet Propulsion Laboratory, California Institute of Technology, Pasadena, CA 91109, USA

List of Figures

8 Tables and figures

Layer	Description	Dimension	After pooling dim. (scat. coef.)	J_ℓ	Q_ℓ	f_ℓ (Nyquist)	$F_\ell = J_\ell Q_\ell$
-1	Raw data (100s, 20 sps)	3 channels × 2000 samples	N/A	N/A	N/A	10 Hz	N/A
0	Decimated data (100s, 10 sps)	3 channels × 1000 samples	N/A	N/A	N/A	5 Hz	N/A
1	First layer	3 ch. × F_1 filters × 512 samples	$3 \times F_1 \times 8$	6	6	1.25 Hz	36
2	Second layer	3 ch. × ($F_1 \times F_2$) filters × 128 samples	$3 \times F_1 \times F_2 \times 8$	7	2	0.312 Hz	14
3	Third layer	3 ch. × ($F_1 \times F_2 \times F_3$) filters × 32 samples	$3 \times F_1 \times F_2 \times F_3 \times 8$	7	2	0.079 Hz	14

Table 1. Computational dimensions of the scattering coefficients. Raw 20 sps data (layer -1) are first decimated to 10 sps for faster computation. A data window of 100 seconds from 3 channels contains 1000 samples per channel at the 0 layer (input layer). After convolving the signal with the F_1 filters of the first wavelet bank, the signal is decimated down to 512 samples. Then, successive decimations by 4 with a 4^{th} order Butterworth anti-alias filter are made from one layer to the next one, ending up to 512, 128 and 32 samples for layers 1, 2 and 3 respectively. We finally obtain the scattering coefficients with an adapted pooling operation performed on all layers at once. The pooling factor is larger at first layers (from 512 to 8 samples) and lower at last layers (from 32 to 8 samples). We finally end up with a number of 8 samples in the time dimension, corresponding to a time resolution of 12.5 seconds in our case. Note that the dimension of the scattering coefficients grows exponentially with the number of filters per layers (F_ℓ) and the number of layers ℓ. J_ℓ, Q_ℓ and f_ℓ defined the network hyperparameters used in this study and defined in both section 2.4 and 4 in the main text.

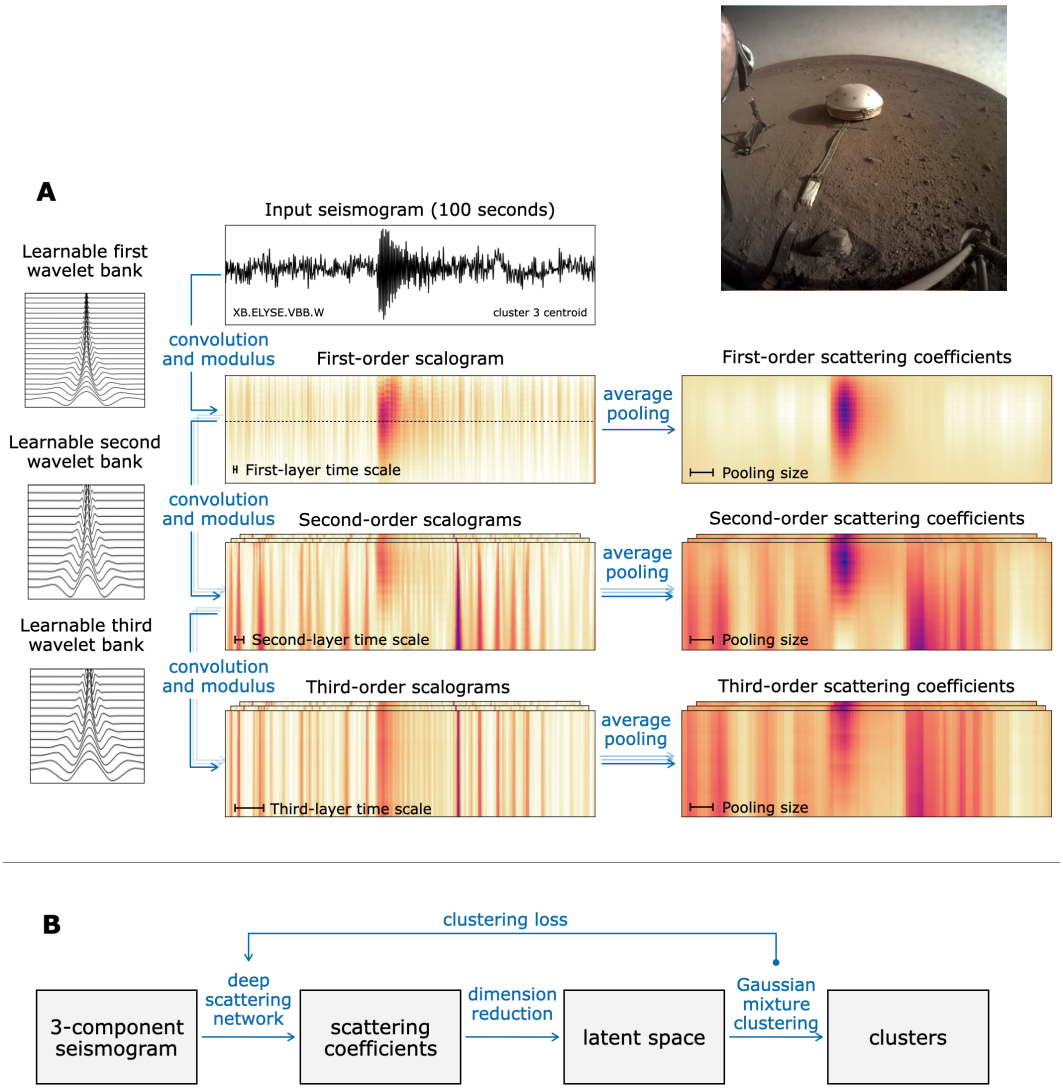

Figure 1. Clustering continuous seismograms with deep scattering network (DSN) and Gaussian mixture model (GMM). A. Deep scattering network the modulus of convolution between the input seismogram and a first learnable wavelet bank defines the first-order scalogram. The average pooling in the time dimension of this scalogram provides the first-order scattering coefficients. The second-order scalograms are obtained from each scale of the first-order scalogram, similarly leading to second-order scattering coefficients with average pooling (Andén & Mallat, 2014). This procedure can be performed at higher orders, and the collection of all-orders scattering coefficients define the scattering representation of the seismic data. The analysis of multiple channels in done by the concatenation of the scattering coefficients obtained for each channel.**B. Clustering workflow** as defined in Seydoux et al. (2020): the scattering coefficients are extracted from the continuous multi-component seismograms with a DSN (illustrated in B). A low-dimensional representation (latent space) of the continuous seismic data is obtained from the first few principal components of the scattering coefficients. The clustering is performed onto the data projected in the latent space with a GMM, allowing to assign a cluster to each segment of signal. The overall strategy optimizes the mother wavelets of each DSN layers to minimize the GMM clustering loss.

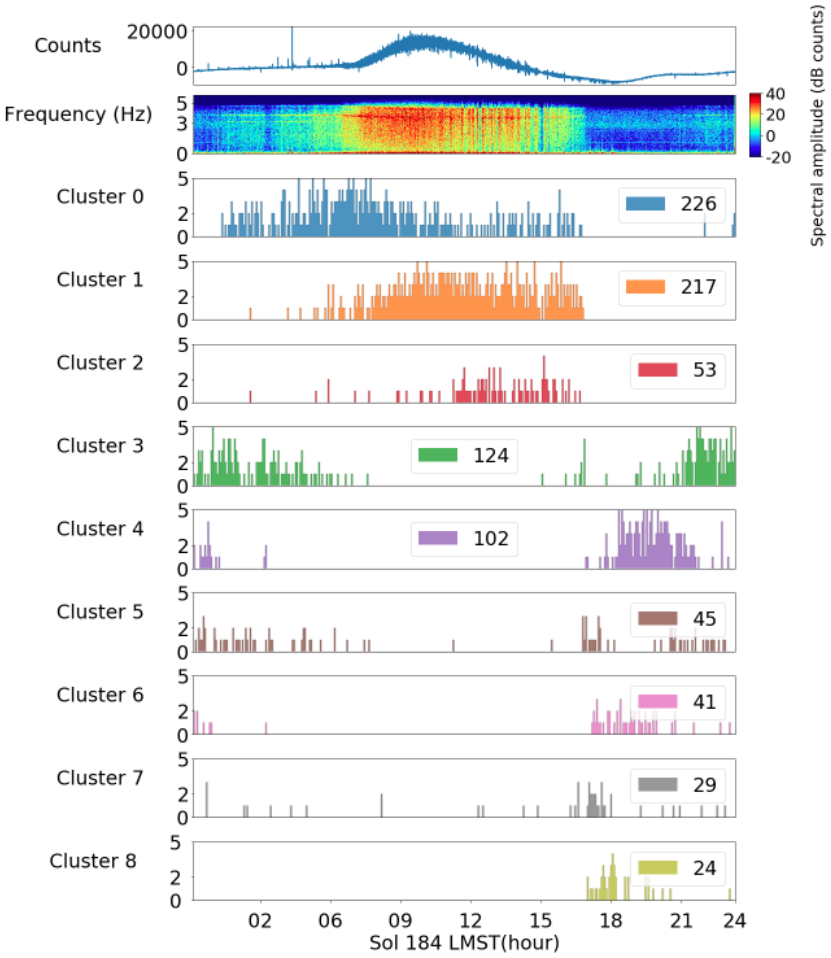

Figure 2. Cluster occurrence frequency on Sol 184. The first panel from the top shows the raw VBB U data for Martian Sol 184. The second panel is the associated spectrogram, computed with a window of 102.4 s, illustrating the evolution of the frequency content. The other panels show the histograms of cluster activities. They give the number of events occurring in an 11-minute window as a function of LMST (Local Mean Solar Time). Numbers on the top right of each panel are the total number of events for that sol.

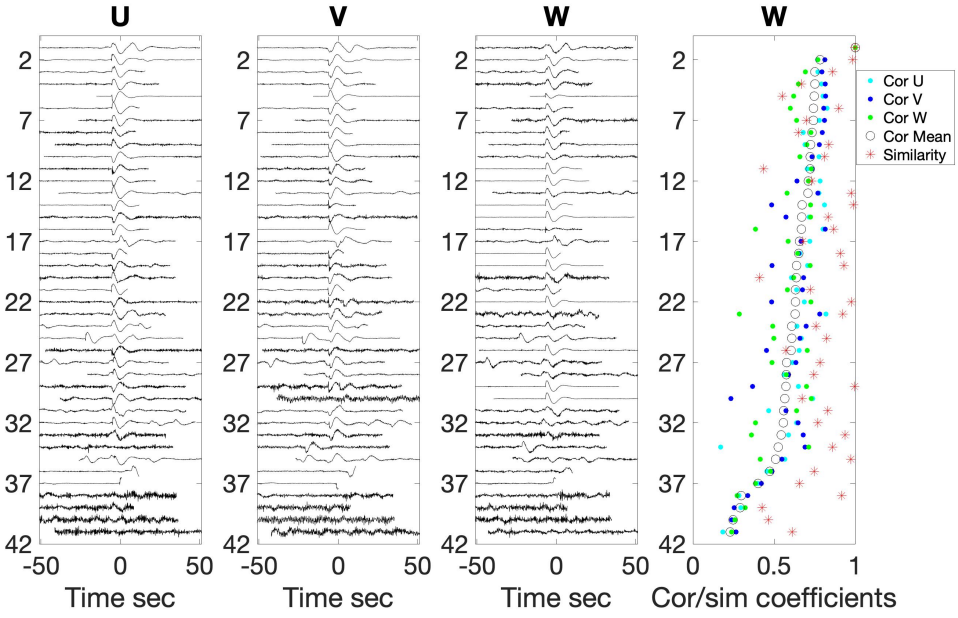

Figure 3. Cluster 6 events aligned on their largest amplitude for the three components. Starting from left to right panels: U, V and W. The top traces are the reference waveforms and the ranking from top to bottom corresponds to decreasing correlation. All waveforms are normalized with respect to their maximum amplitude and event start time is at t=0 s. Correlation is defined as the mean value of the 3 correlation obtained for each axis, and is shown on the right panel as a circle. The three values of correlations for U, V, W are also shown as colored dots on this right panel, together with similarity with a red stars, plotted to the power 1/6 due to the 6 dimension of the manifold. As clustering is done with a mixture of noise level and waveform similarities, correlations and similarities are not correlated.

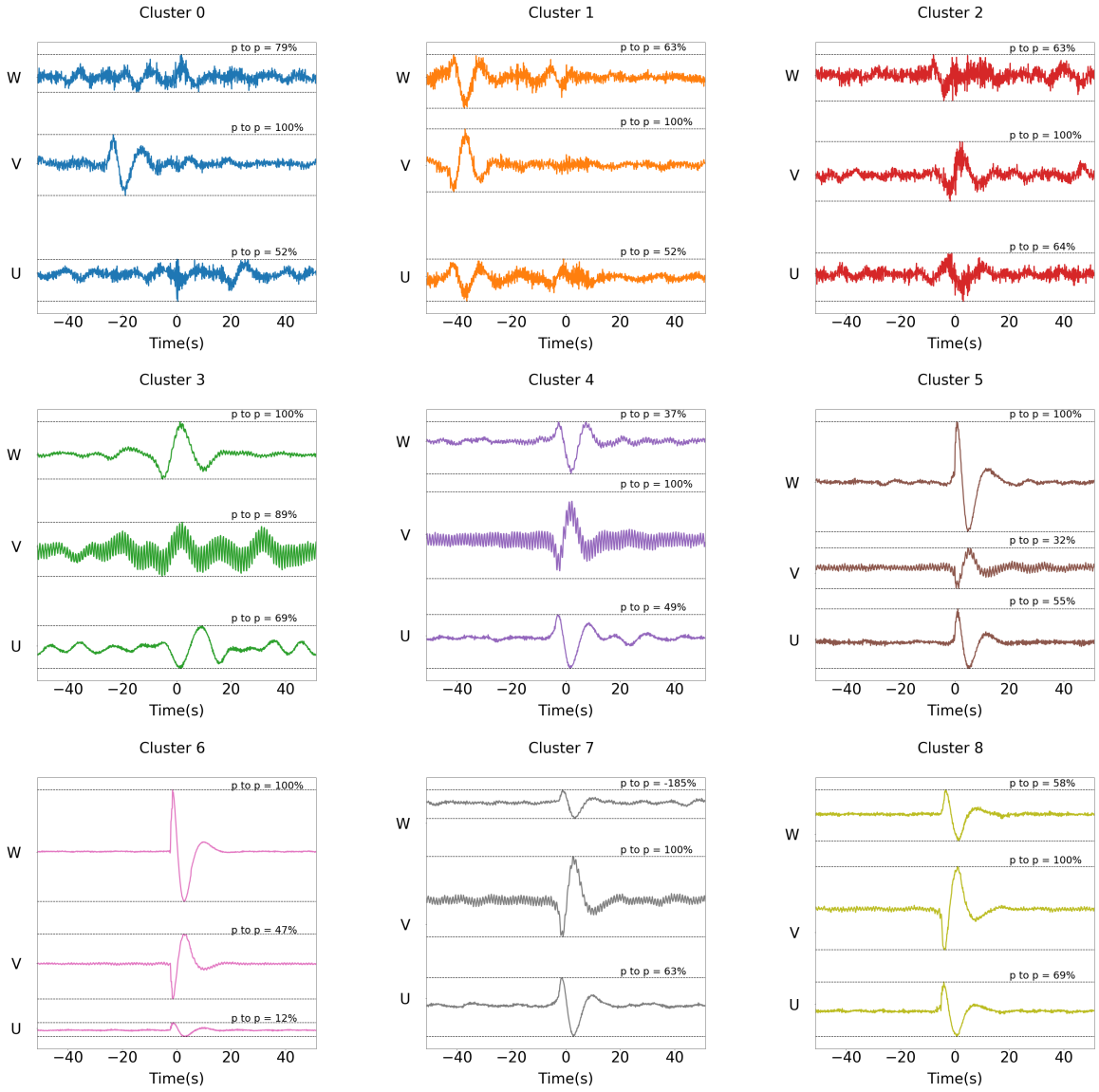

Figure 4. Centroid waveforms of the 9 clusters. For each cluster, the waveforms of the 3 components U, V and W are plotted together with the corresponding peak to peak percentage computed with respect to the component with the maximum amplitude. This provides the relative amplitude of the three components, a feature taken into account in the clustering process. Amplitudes are normalized by the mean squared norm L_2 applied on the 3 axis. The cluster event starts at 0 s (centered using the same procedure explained in figure 3).

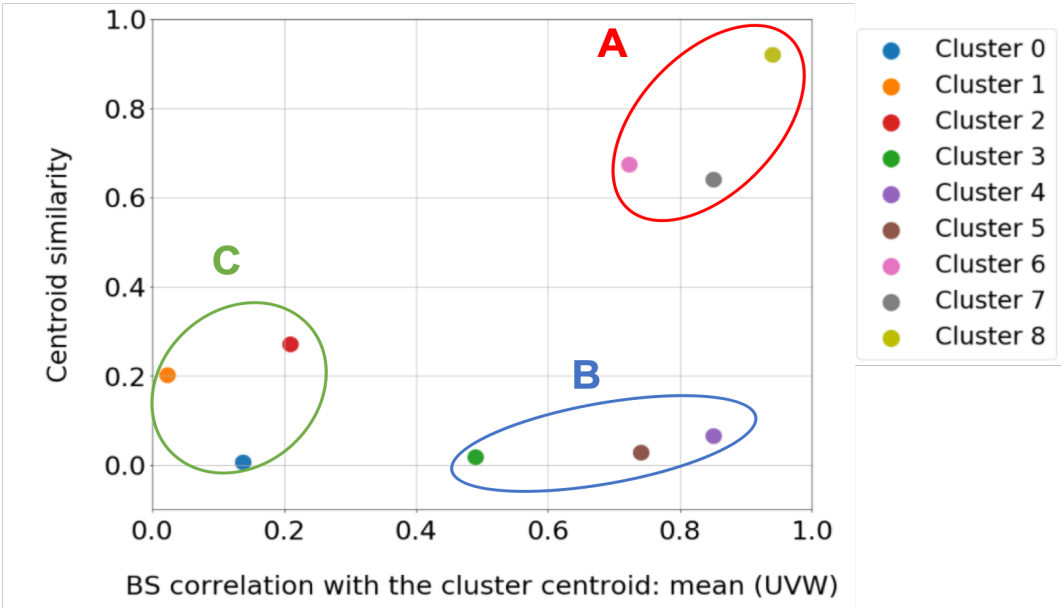

Figure 5. Cluster's centroid similarity distribution in function of its correlation with the best similarity event for each cluster . This figure highlight 3 families A, B and C: family A in red : During the clustering procedure, the waveform shape is the dominant feature. Family B in blue: the waveform is not the only main feature used in the clustering (e.g. the background noise, the relative amplitude...). Family C in green: the background noise is the dominant feature during the clustering procedure. It is more related to the response of the external Martian sources in the seismic data, like the background noise generated by pressure drops (cluster 0 and 1) or wind burst (cluster 3).

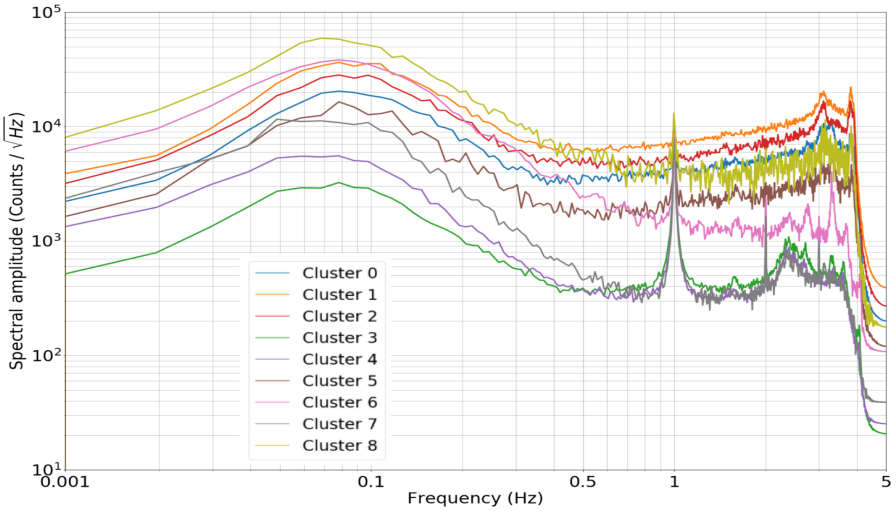

Figure 6. Amplitude spectral density of the 9 cluster centroid waveforms for the V component.

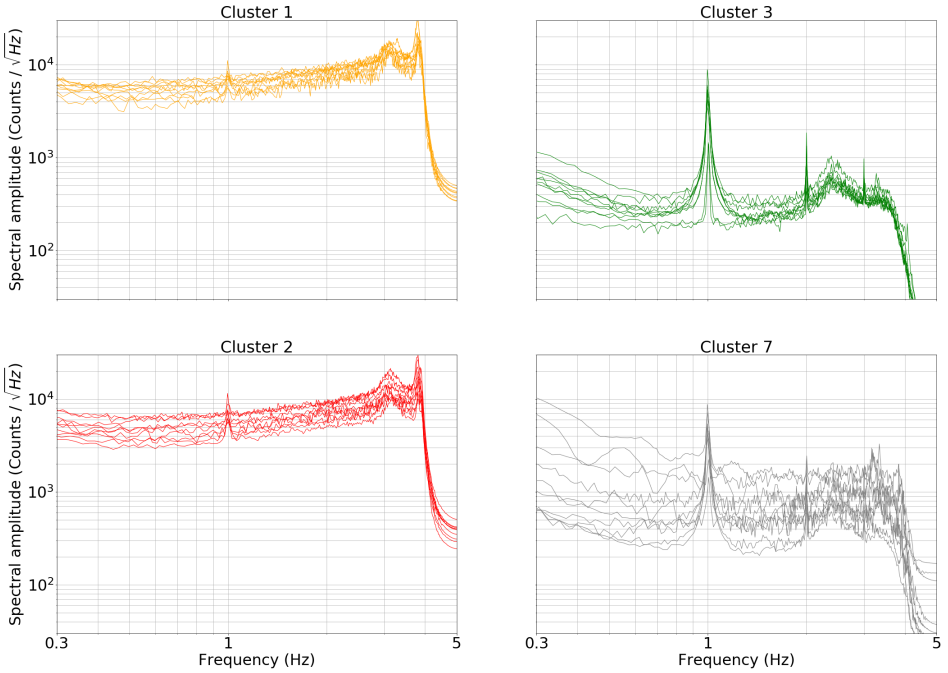

Figure 7. Stable cluster spectrum. Each plot shows the centroid spectra of the clusters 1, 2, 3 and 7, as obtained from learning on the following Martian Sols: Sol193, Sol203, Sol213, Sol223, Sol234, Sol243, Sol253, Sol363, Sol372, Sol393. These cluster's events have 95% similarity between each others.

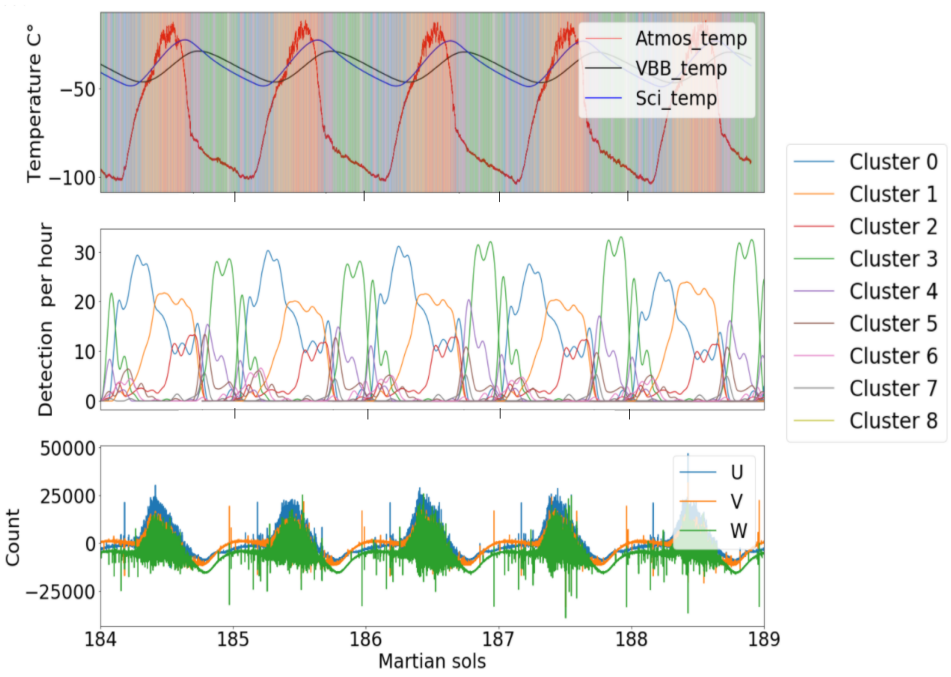

Figure 8. Temperature correlation. Top panel: Temperature (in Celsius) recorded at three different locations. On the lander (outside temperature in red), under seismometer thermal shielding (scientific temperature in blue), next to the VBB U sensors (VBB temperature in black). For each local hour, the color in the background corresponds to the cluster which has the maximum number of detection, as shown in the bottom plot. Middle panel: Number of detection per hour for the 9 clusters. Each color line corresponds to one cluster with the same color code as in Figure 7 (0: blue, 1: orange, 2: green, 3: red, 4: purple, 5: brown, 6: pink, 7: gray, 8: gold). Both plots are a function of local time in sols, from sol 183 to sol 189. Bottom panel: U, V and W raw data presented from Sol 184 to Sol 189.

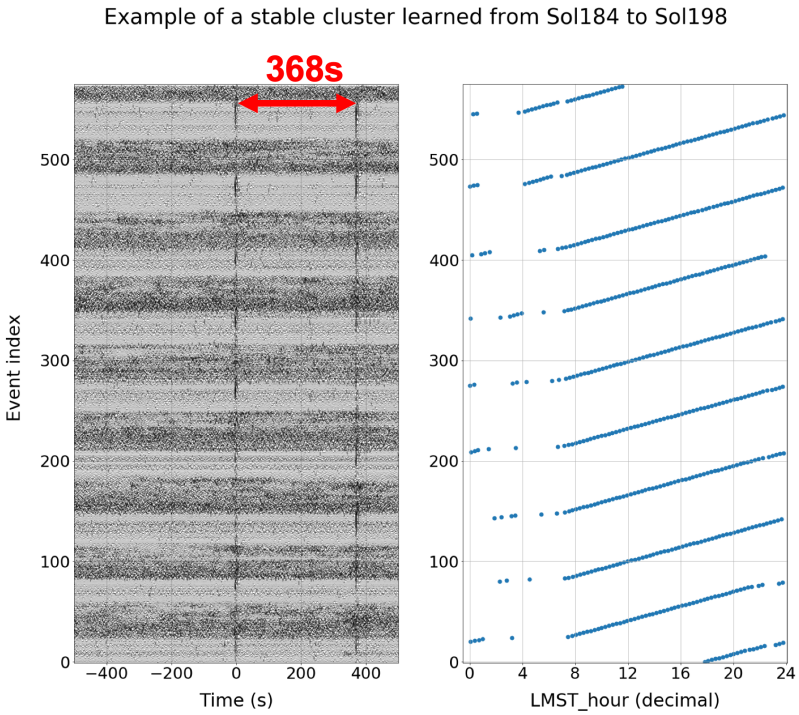

Figure 9. On the left, cluster of doublet glitches with 368 s time delay on component W. Amplitudes are normalized as in Figure 4 and RMS is 2.3 s. The right panel provides the LMST of these glitches and shows that an interruption is observed during the coldest time of the night.

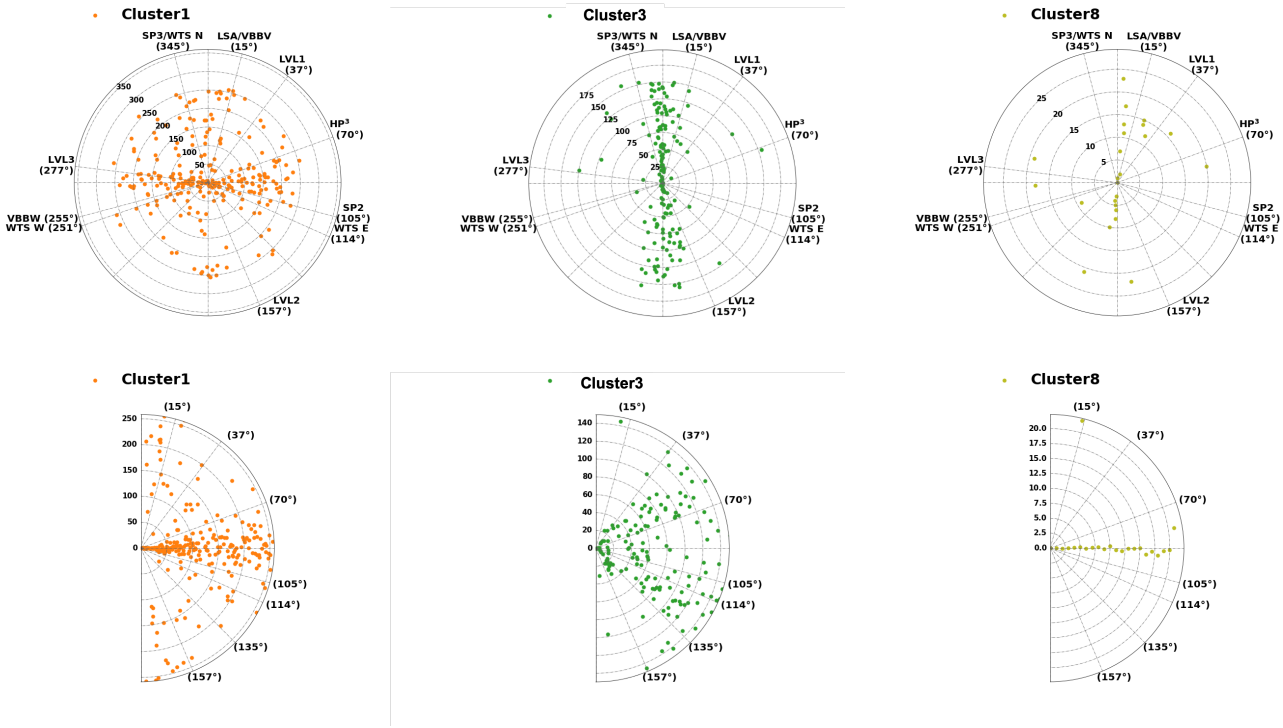

Figure 10. Back azimuths and dip of the events of clusters 1, 2 and 8 recorded on sol 183. The first 3 plots on the top shows the back azimuth of the clusters 1,2 and 8. For each cluster, the corresponding events are plotted with points as a function of their back azimuth from 0 to 360^o along the outer circle and as a function of their index along the radius. The events are assumed to be linearly polarized. The inner dashed circles give the event indices. Events in the center have the best similarity with the cluster centroid. Note that these numbers are different for each cluster. Azimuths related to the SEIS instrument feature are given on the outer circle and include: the sensitivity azimuth of the VBB (U, V, W) and SP sensors (SP2,SP3), the feet of the LVL system (LVL1-2-3), the feet of the Wind Thermal Shield sub-system (WTSE, W, N) and the Load Shunt Assembly (LSA). SP1 is not listed since this is the vertical component SP sensor. The three figures in the bottom illustrates the dip of 1,2 and 8 clusters following the same representation as the azimuth.

Figure 11. Waveforms of pressure drop clusters. The stacked waveforms are obtained using the approach outlined in Section 4.

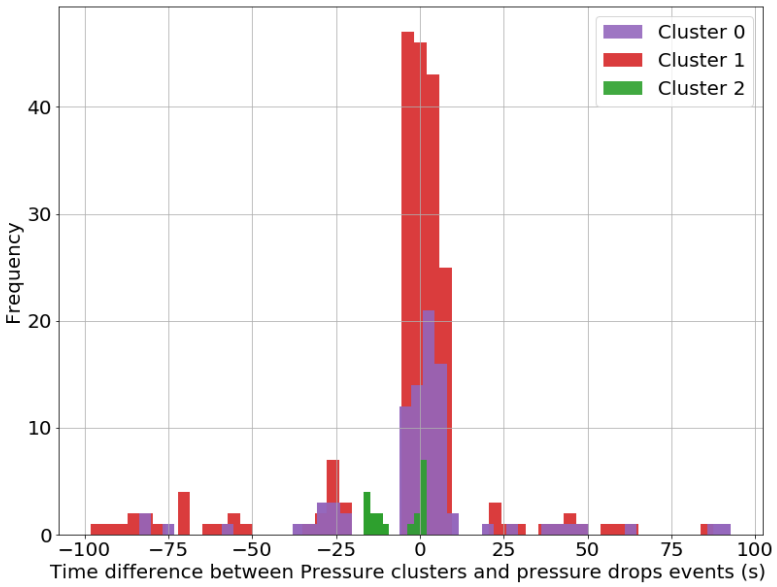

Figure 12. Timing of pressure drops. Histogram showing the number of pressure drops as a function of time difference between the pressure drop center, as reported in the pressure drop catalog of Spiga et al. (2021) and the center of the pressure drop, as event of cluster 0, 1 and cluster 2. The bin size is 4 s for cluster 0 and 1 and 2 s for cluster 2. The learning window is 100 s and the difference are reported when within ±100 s.

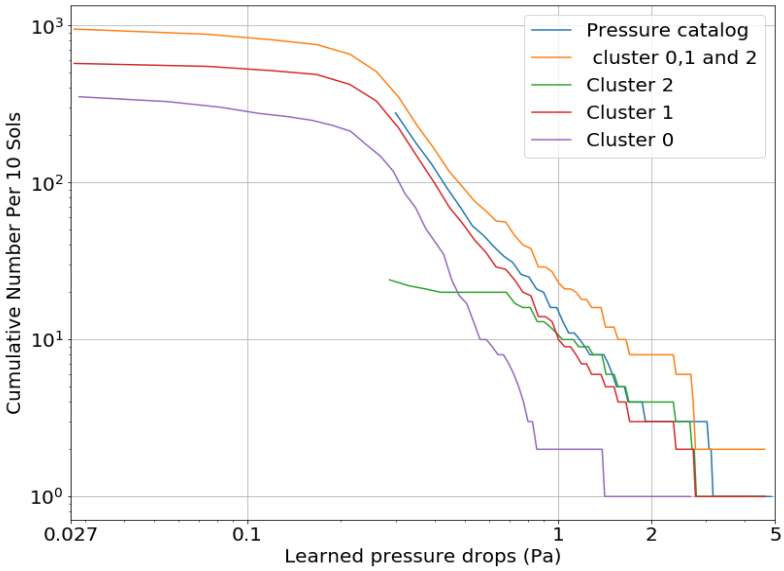

Figure 13. Statistics of pressure drops. Cumulative histogram of the pressure drops from Spiga et al. (2021) catalog (blue) and for the combined clusters 0-1-2 (orange). The histograms for each pressure drop cluster are also provided, with colors purple, red and green for 0,1,2 respectively.

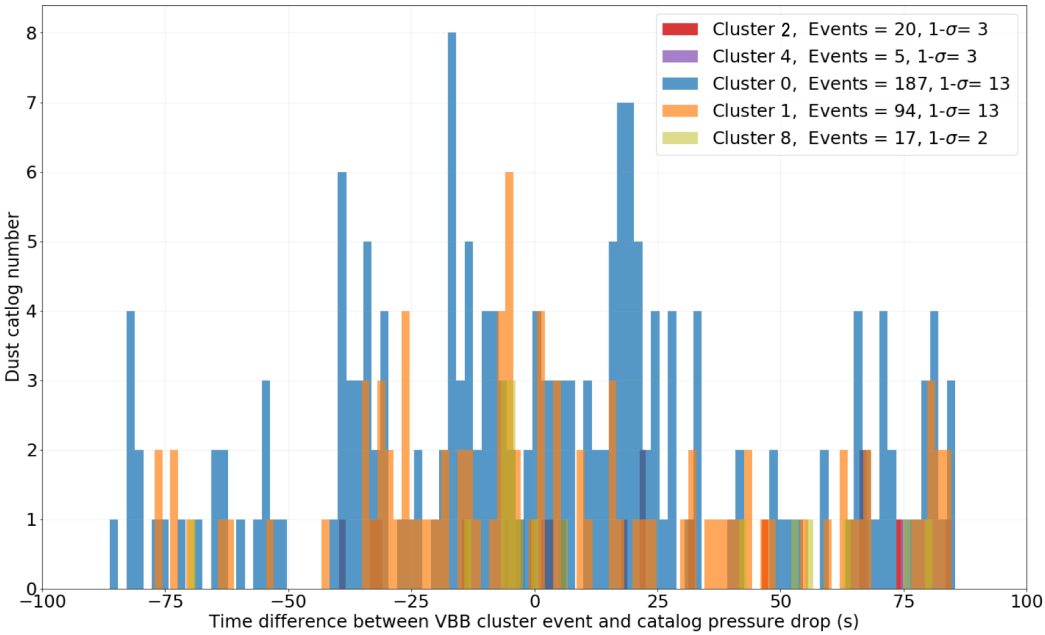

Figure 14. VBB pressure drops statistics. Histogram showing the number of pressure drops as a function of time difference between the pressure drop center, as reported in the pressure drop catalog and the center of the VBB events of several clusters. The learning window is 100 s and the difference are only reported when within ±100 s. Only clusters for which the number of coincidence is larger than the 1-σ value obtained for random process are shown.

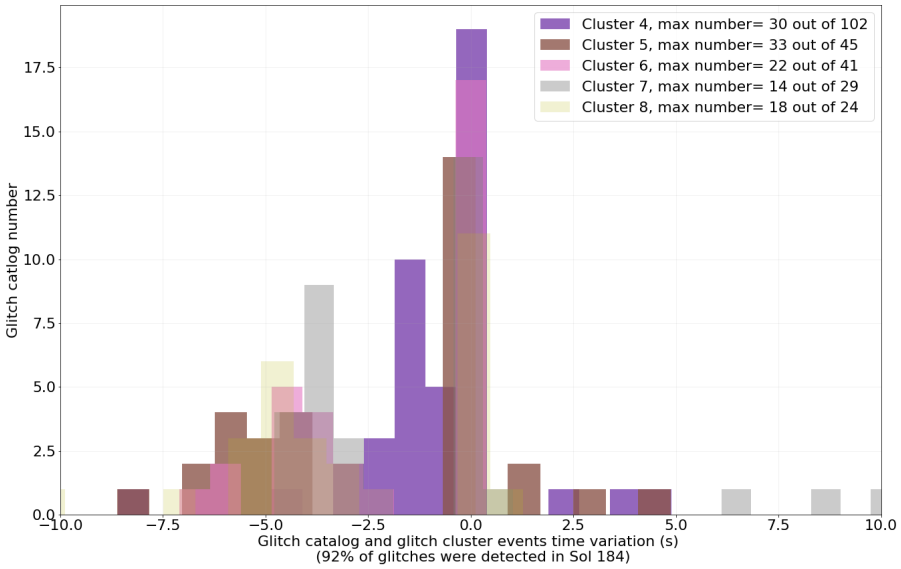

Figure 15. Glitch detection timing. Histogram showing the time difference of glitches cataloged by Scholz et al. (2020) and the glitch clusters. Only differences smaller than 10 s are shown in Sol 184. 127 glitches are listed in catalog. In the figure's legend, we mention the total number of glitches for each cluster out of its total event's number.

Appendix A Clusters' waveforms

In this appendix, we show the clustering results for all the clusters and associated events obtained on sol 184 used for computing centroids. All these events can be found, together with their occurrence time, cluster type, amplitude on U,V,W, similarity coefficient and correlation coefficient with respect to the cluster's reference event in e-supplementary material available in the folder AppendixA-VBBClusters available at: https://www.dropbox.com/sh/2vnaepwmle8nm60/AACT3OctWtEOZxVDHbfFF9Iga?dl=0

First, we illustrate below the centroid spectrum of the two VBB component U and W respectively in Fig A1 and Fig A2, the V component being in the main text. The clusters figures shown in Fig A3, A4, A5, A6, A7, A8, A9, A10, and A11, illustrate all the events waveforms aligned for each cluster over the reference period in addition to their similarity and correlation coefficient computed in the same procedure as in figure 3 of the main text.

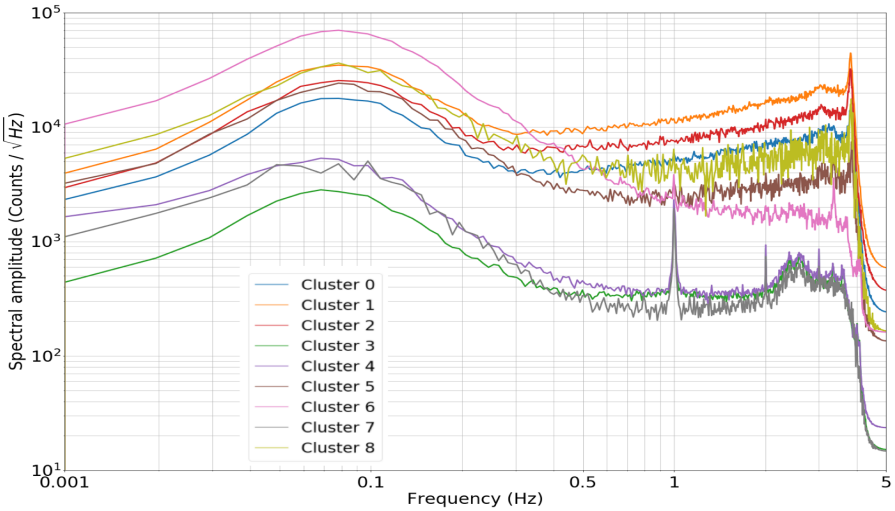

Figure A1. Amplitude spectral density of the W component clusters centroid.

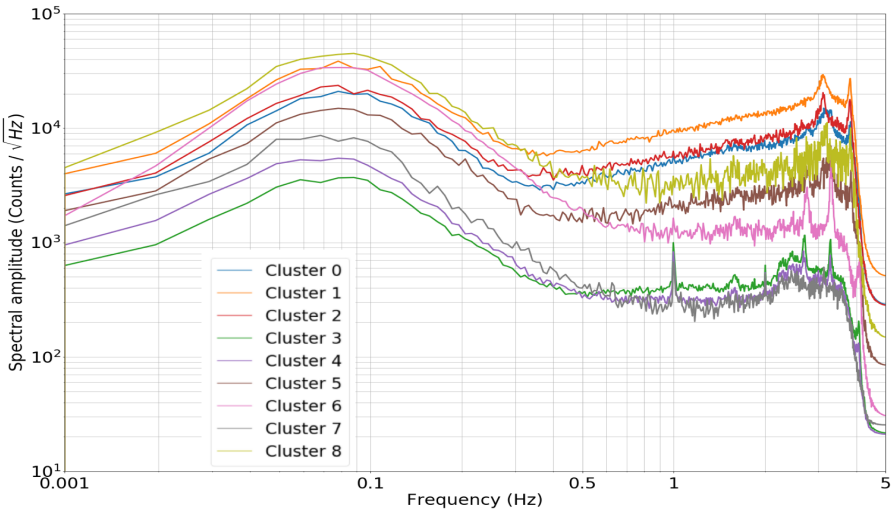

Figure A2. Amplitude spectral density of the U component clusters centroid.

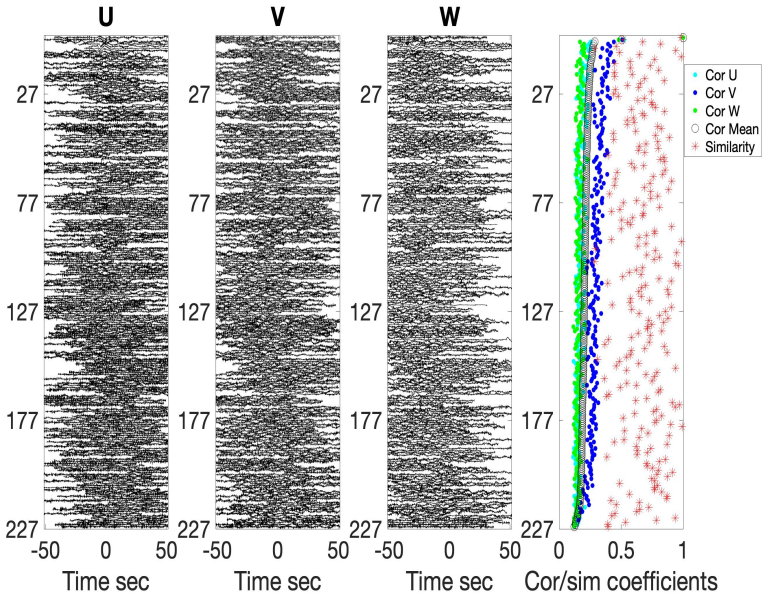

Figure A3. Cluster 0 aligned waveforms. The 3 first figures from left to right shows all the cluster 0 events waveforms aligned to a chosen reference respectively of U,V and W component.The 4th figure illustrates the similarity coefficient (plotted to the power 1/6 due to the 6 dimension of the manifold) as well as the correlation coefficient defined as explained in figure 3

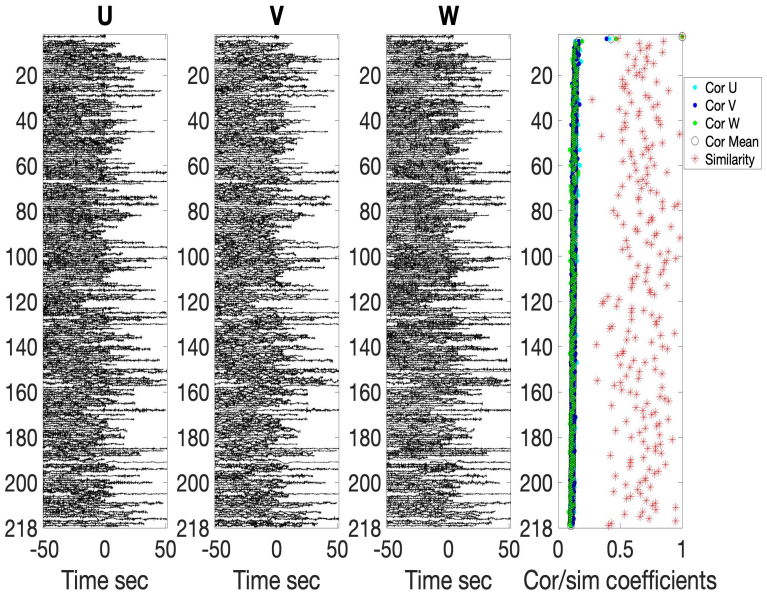

Figure A4. Cluster 1 aligned waveforms. Same as A3 but for cluster 1.

.

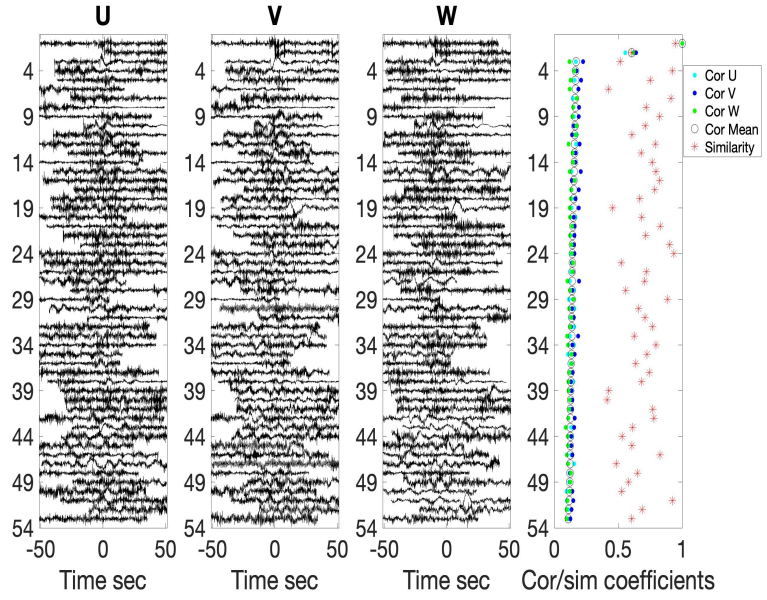

Figure A5. Cluster 2 aligned waveforms. Same as A3 but for cluster 2.

.

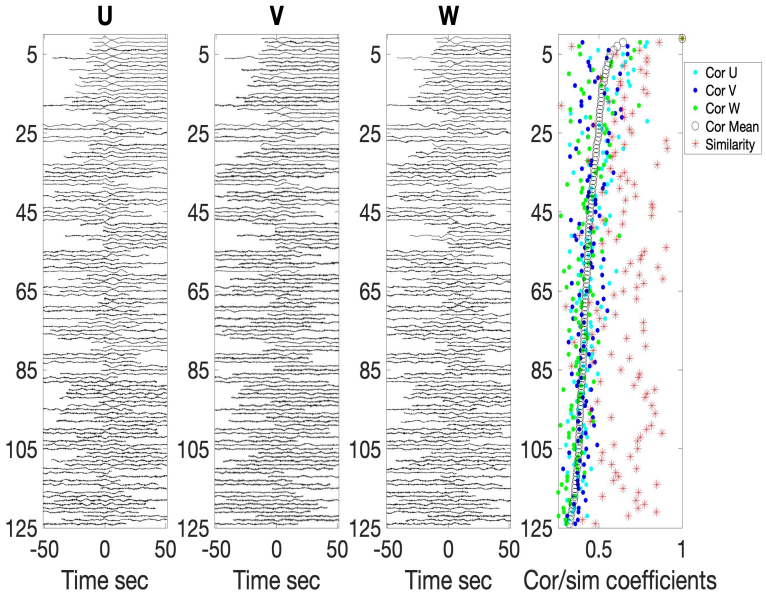

Figure A6. Cluster 3 aligned waveforms. Same as A3 but for cluster 3.

.

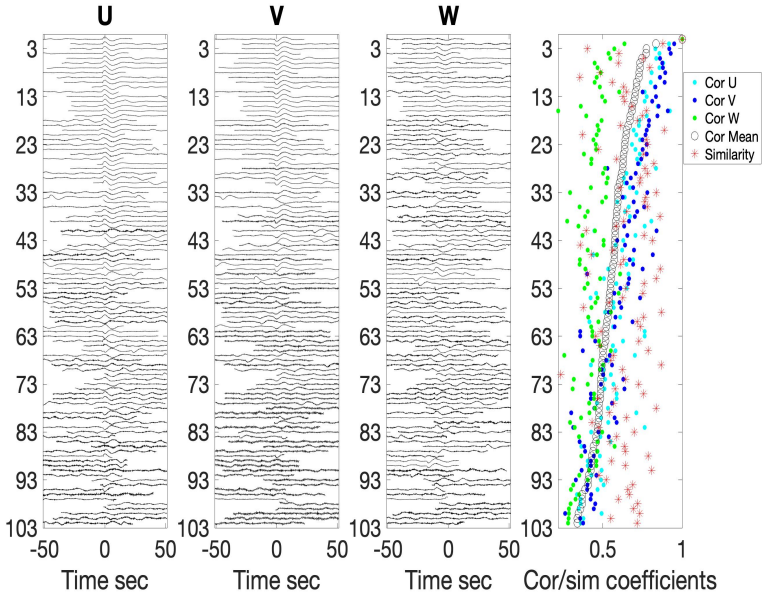

Figure A7. Cluster 4 aligned waveforms. Same as A3 but for cluster 4.

.

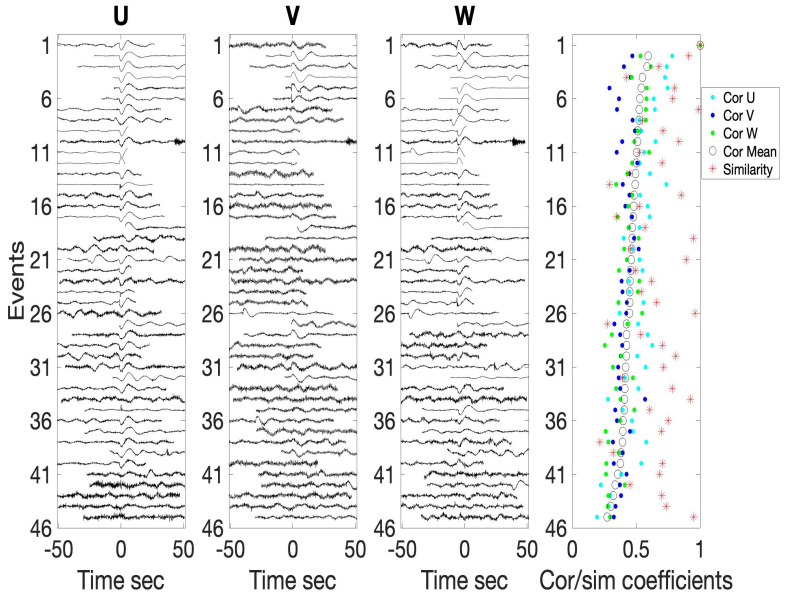

Figure A8. Cluster 5 aligned waveforms. Same as A3 but for cluster 5.

.

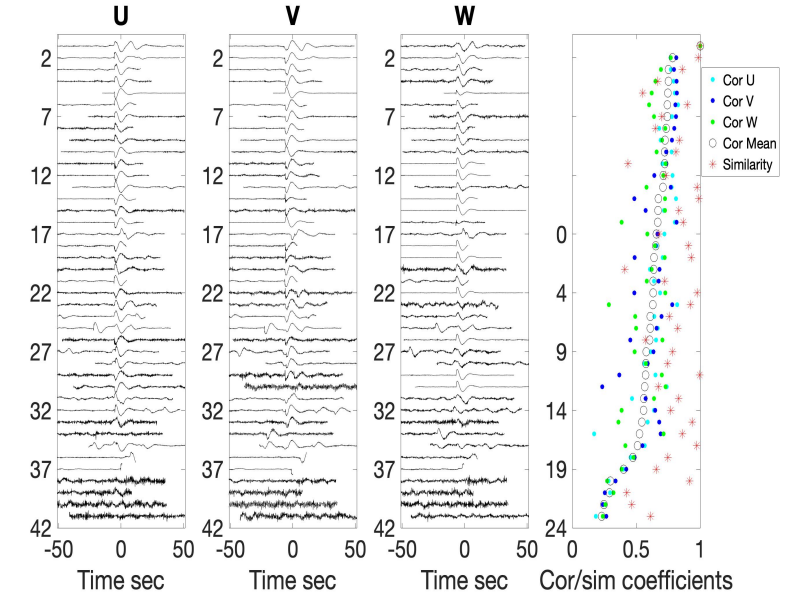

Figure A9. Cluster 6 aligned waveforms. Same as A3 but for cluster 6.

.

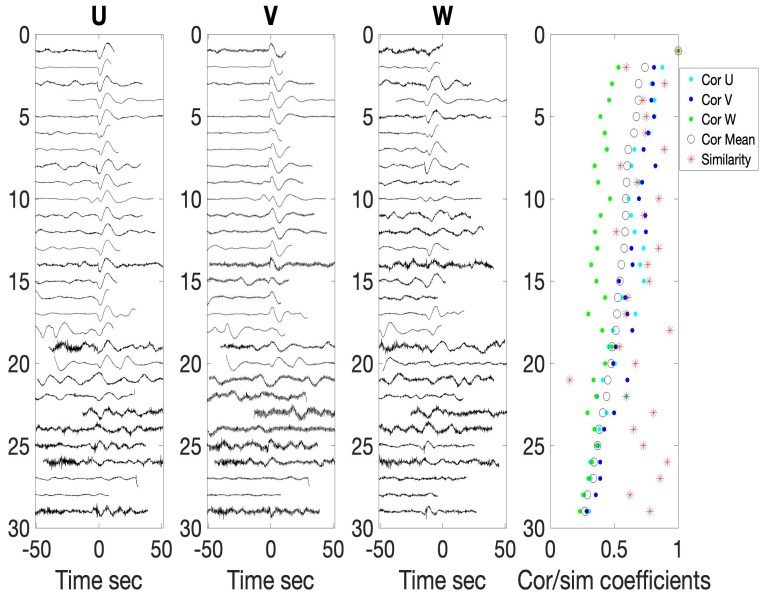

Figure A10. Cluster 7 aligned waveforms. Same as A3 but for cluster 7.

.

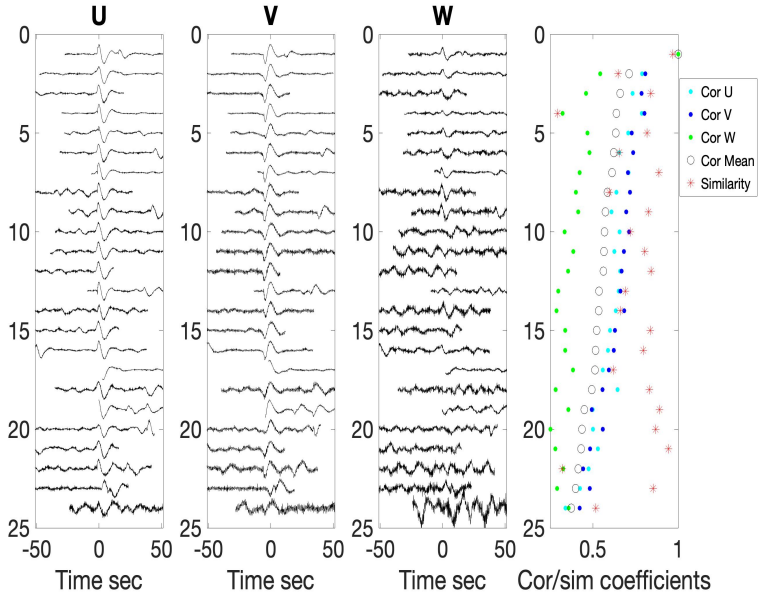

Figure A11. Cluster 8 aligned waveforms. Same as A3 but for cluster 8.

.

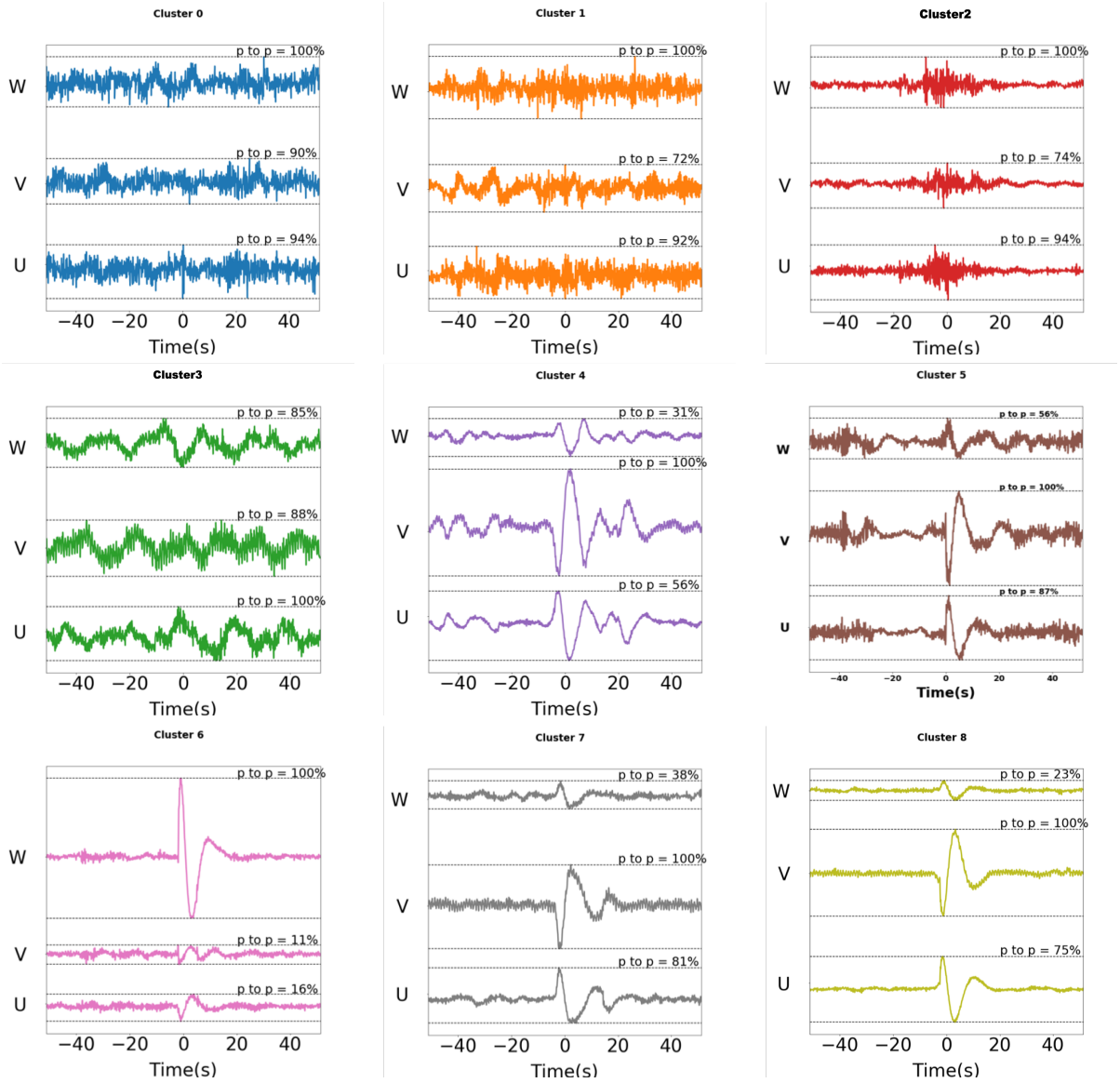

Figure A12. Best similarity waveforms of the 9 clusters. For each cluster, the waveforms of the 3 components U, V and W are plotted together with the corresponding peak to peak percentage computed with respect to the component with the maximum amplitude. This provides the relative amplitude of the three components, a feature taken into account in the clustering process. Amplitudes are normalized by the mean squared norm L_2 applied on the 3 axis. The cluster event starts at 0 s (centered using the same procedure explained in figure 3).

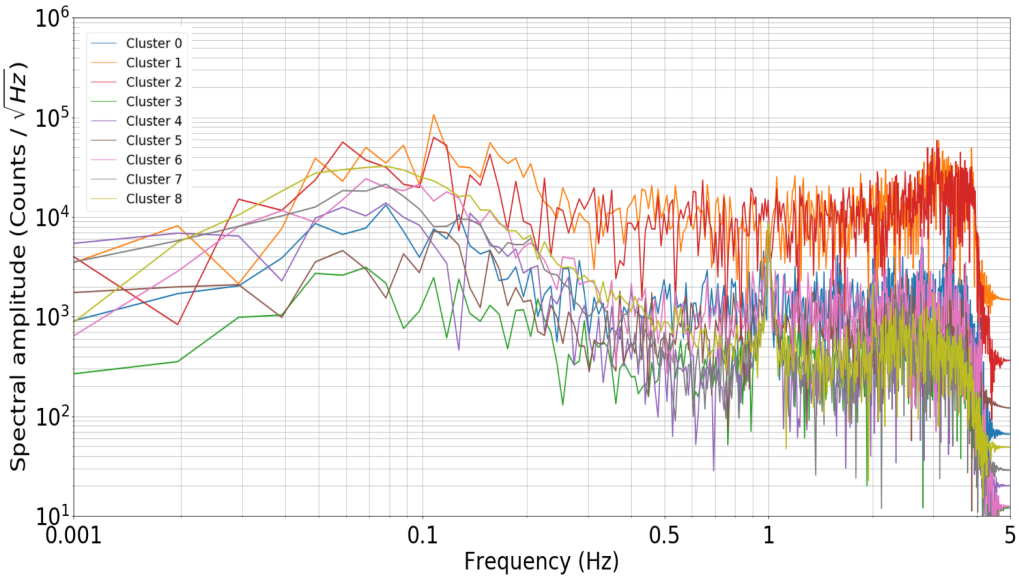

Figure A13. Amplitude spectral density of the V component of the clusters best similarities events.

Appendix B Extended time window and clustering of tuplet glitches

In this section, we show the performance of DSN to learn and track stable glitch sequences with stable time offset in further different period (April and June) to illustrate the stability of the learning process. During both test, we applied the same DSN configuration on 2sps U,V and W VBB data.

B1 April learning results

In this section, we illustrate the clusters obtained after the learning process with stable time offset as shown in figure B1. In this test, we used a larger learning window : 512s and kept the same configuration. The learning period was from 2019-03-31, 23:57:26 UTC to 2019-04-15, 00:00:02 UTC (2 weeks).

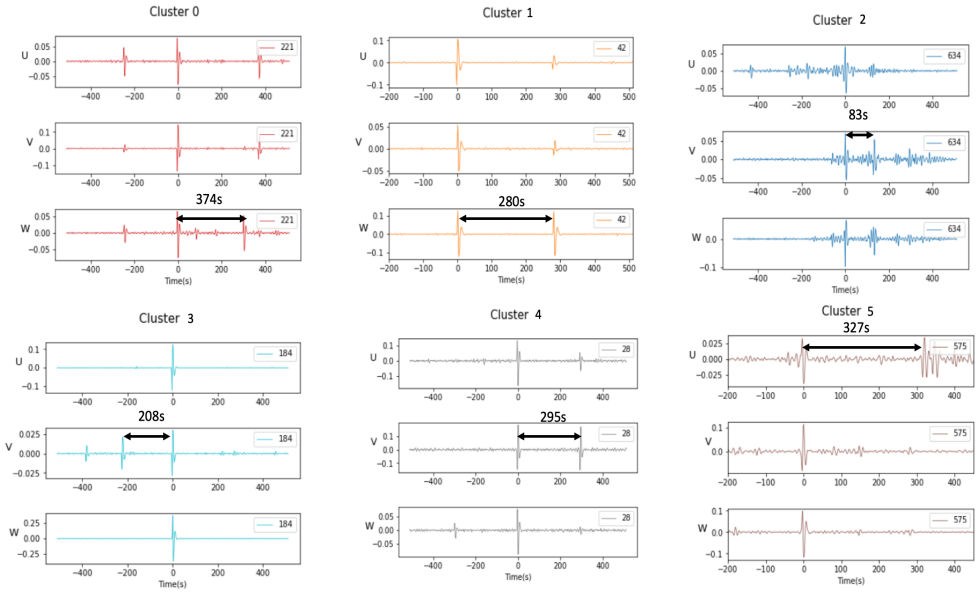

Figure B1. Glitches sequences clusters obtained in April: The obtained time offsets are 374s, 280s, 327s, 295s, 208s and 83s with RMS respectively equal to 0.09s, 0.98s, 1.07s, 0.96s, 2.36s and 0.12s

B2 June learning results

To check the capability and the stability of the learning process, we run the same test with the same window (512s) but in June from the 2019-06-10T00:00:00 UTC until 2019-06-23T23:59:50 UTC(2 weeks). Its results are summarized in figure B2.

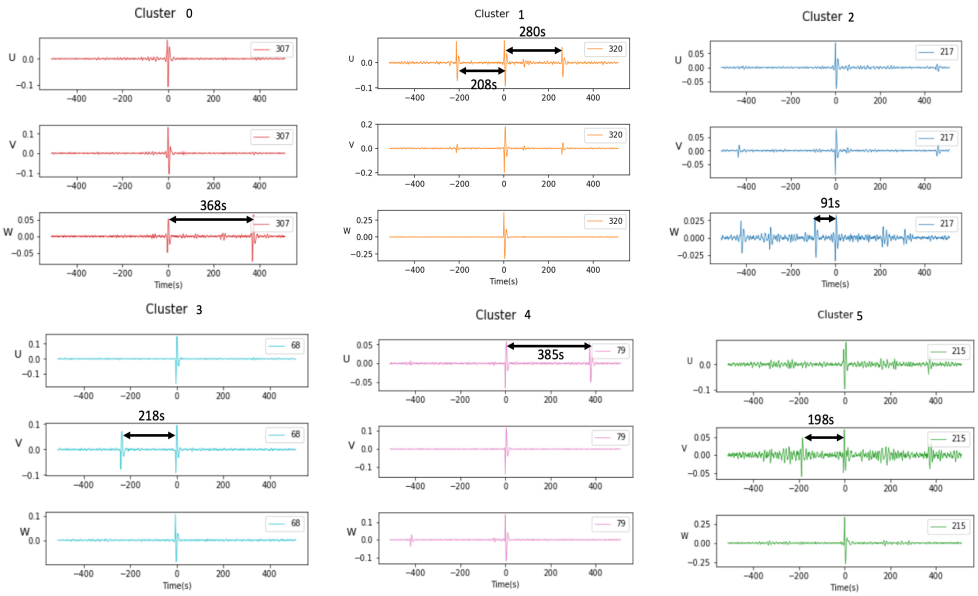

Figure B2. Glitches sequences clusters obtained in June: The obtained time offsets are 368s, 91s, 218s, 385s, 280s, 208s and 198s with RMS respectively equal to 0.09s, 0.98s, 1.07s, 0.96s, 2.36s, 5.63s and 0.12s

Appendix C Waveforms of tuplet glitch clusters

In this appendix, we show all the events of doublet-tuplet glitch sequences clusters with stable delays between consecutive glitches. A Tuplet glitches cluster is shown in figure C1, with a 3D representation of all the events waveforms on the left figure and the associated stack on the right. We detected also multiple doublet as illustrated in figures C2 and C3.

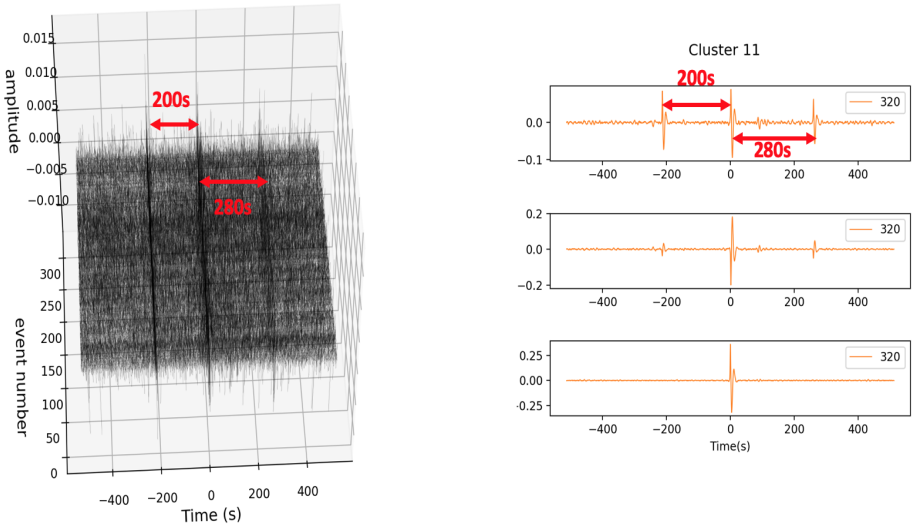

Figure C1. 3D triple glitch cluster 11 obtained in June learning test. In this example, the mean delay and associated rms were computed between the event centered at 0s and the glitch at 280s. Mean delay is 280.9 and RMS is 0.9s

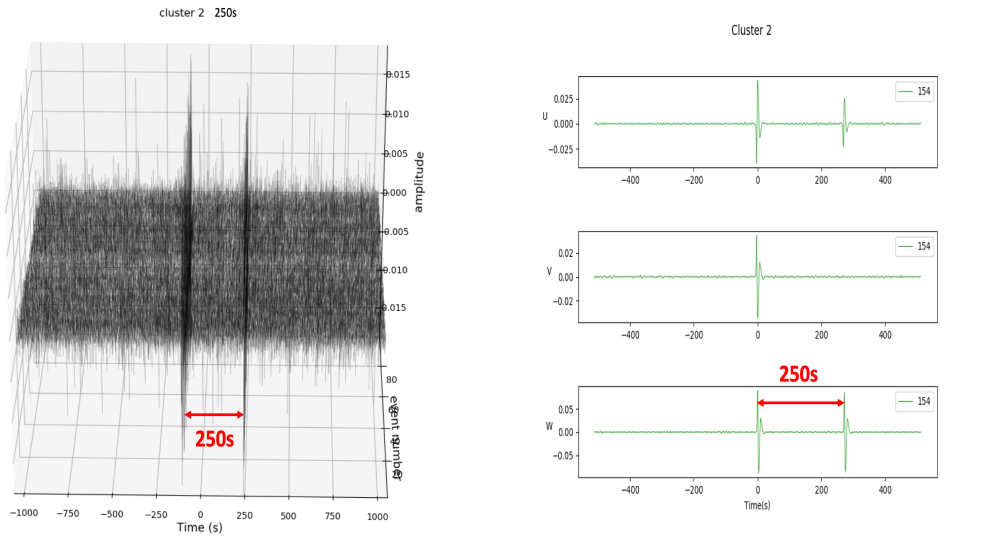

S

Figure C2. 3D double glitch cluster 2. It was obtained in one learning test made for Sol 363. Mean delay is 248.6s with an RMS of 1s.

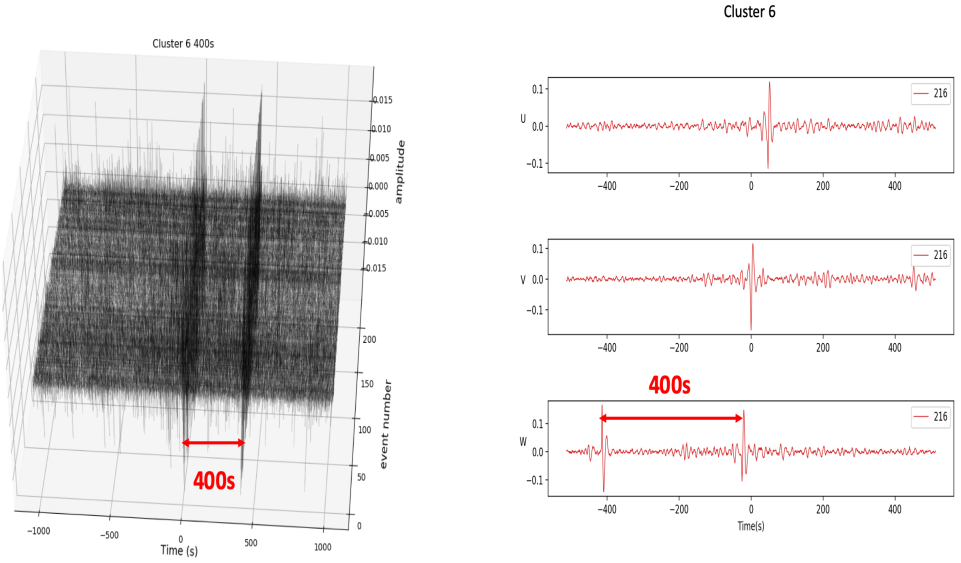

Figure C3. 3D double glitch cluster 6. It was obtained in April learning test. Mean delay is 397.5s with an RMS of 3.9s.

Appendix D Clustering continuous pressure data

In this appendix, we show the clustering results for all the pressure clusters and associated events obtained for the period from June, 2, 2019, 0:00:00 to June, 11, 2019, 0:00:00 for pressure data. All these events can be found, together with their occurrence time, cluster type, amplitude, similarity coefficient, correlation coefficient and event amplitude with respect to the cluster's reference event in e-supplementary material available in the folder AppendixD-PressureClusters available at:
https://www.dropbox.com/sh/2vnaepwmle8nm60/AACT3OctWtEOZxVDHbfFF9Iga?dl=0

During the learning process, we detected 7 clusters in total. Three are identified as pressure drop clusters as shown in the main text. To have a better view of the global results, we first show the pressure clusters distribution in figure D1. Then, we provide their aligned waveforms as well as their corresponding similarity and correlation coefficient in figures: D2, D3, D4, D5, D7, D8 and D9. Events from cluster 0 and 6 show a clear centered event on the aligned waveforms figures. Their waveforms stack is shown in figures D6 and D10 respectively. These clusters correspond to a sharp wind burst seen in the pressure data and also detected by DSN.

For the three pressure drops clusters, we show in figures D2, D3 and D4 and in black the events detected in both the pressure drop catalog made by (Spiga et al., 2021) and the learning catalog in black and in red the events only seen by the learning process.

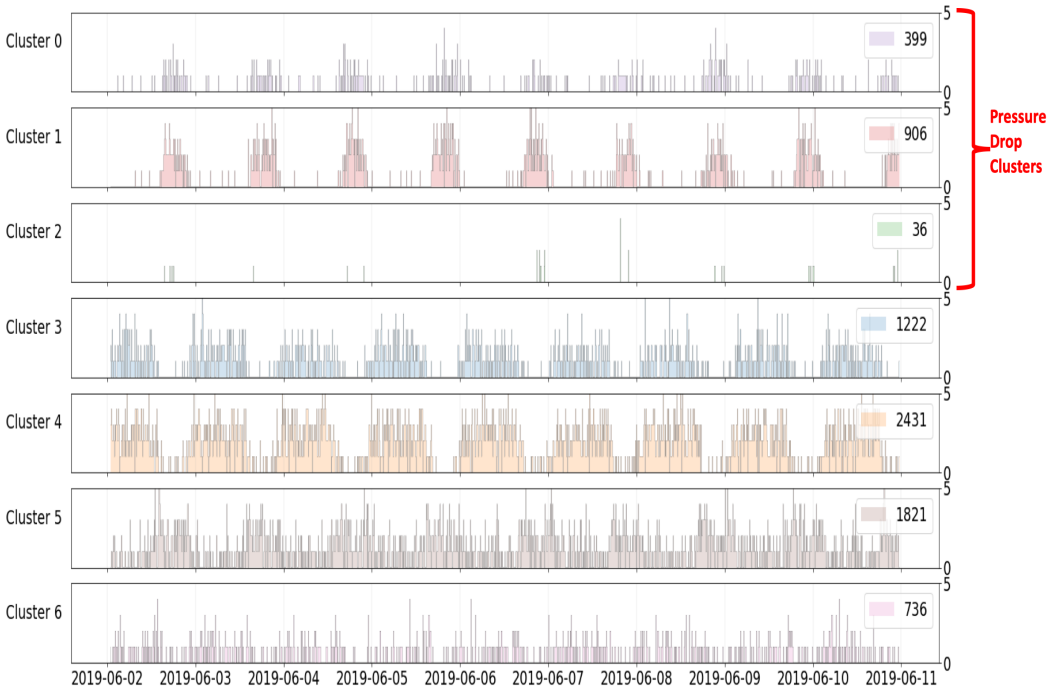

Figure D1. Pressure clusters distribution from the June 2 to June 11. The learning process has detected 7 clusters. Three of them are pressure drop clusters: Cluster 0, 1 and 2. The number of event detected over the period is on top right of each cluster figure.

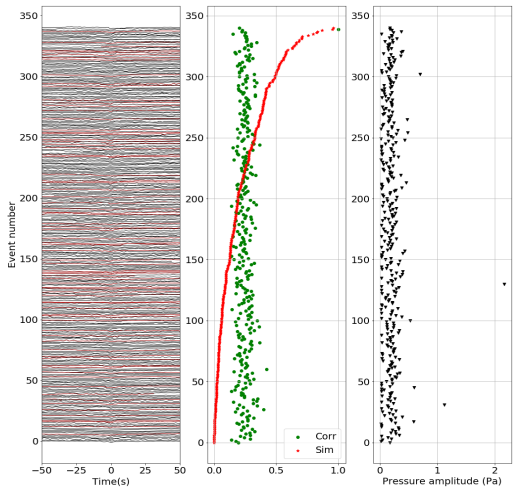

Figure D2. Pressure cluster 0 aligned waveforms: The first figure shows the events waveforms aligned to a chosen reference. The plots in red correspond to the events that are detected also in the pressure catalog. The second figure illustrates the events correlation and similarity power to 1/6 respectively in green and red points. The third figure shows the events pressure amplitude in Pa.

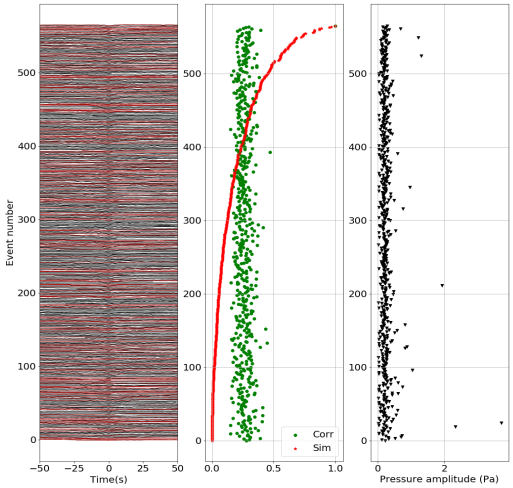

Figure D3. Pressure cluster 1 aligned waveforms: Same as D2 but for cluster 1.

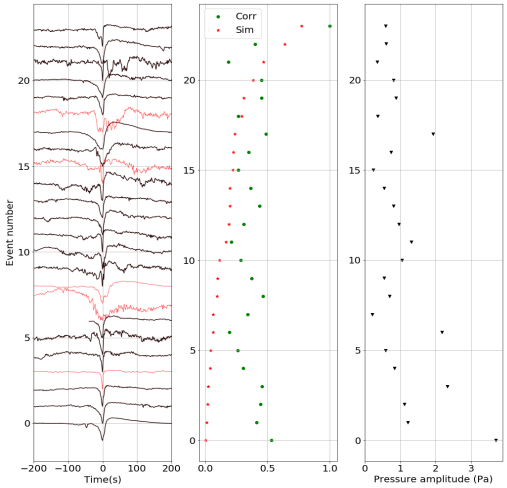

Figure D4. Pressure cluster 2: aligned waveforms. Same as D3 but for cluster 2.

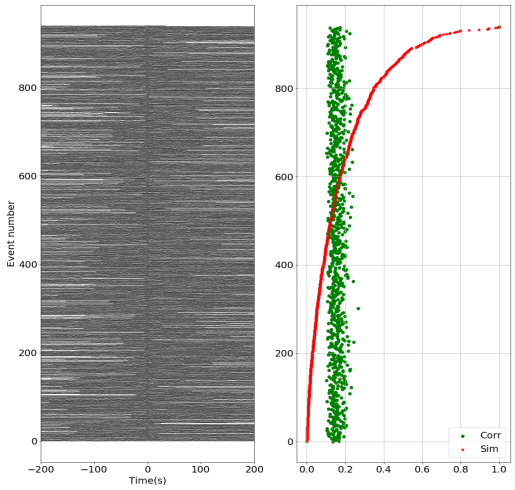

Figure D5. Pressure cluster 3: The figure on the left shows the aligned waveforms, with decreasing similarity coefficient from top to bottom. The figure on the right shows, for all events, the similarity coefficient and the correlation with the highest similarity event.

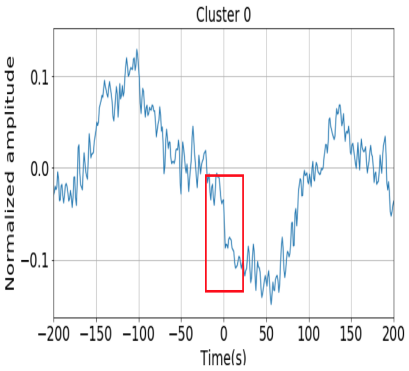

Figure D6. Pressure cluster 0 stack waveform.

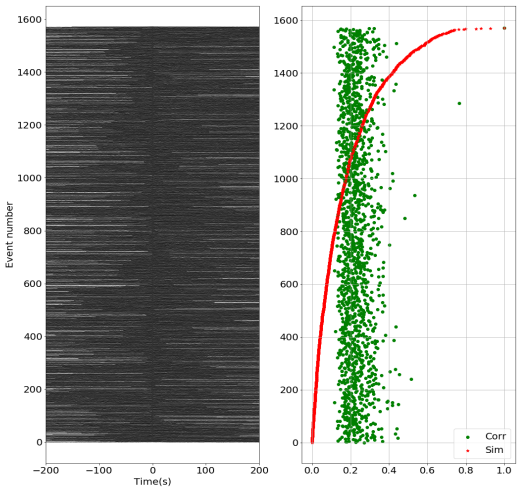

Figure D7. Pressure cluster 4:. Same as D5 but for cluster 4.

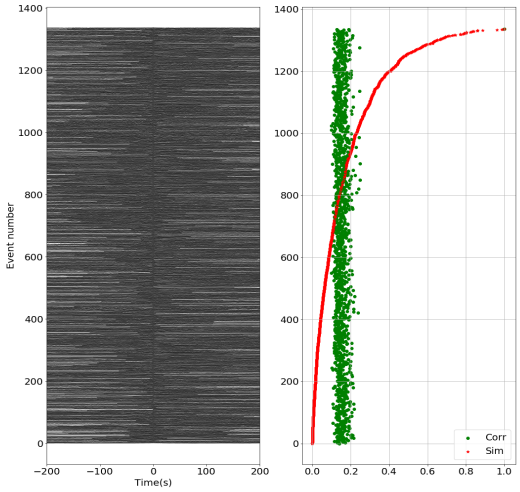

Figure D8. Pressure cluster 5: Same as D5 but for cluster 5.

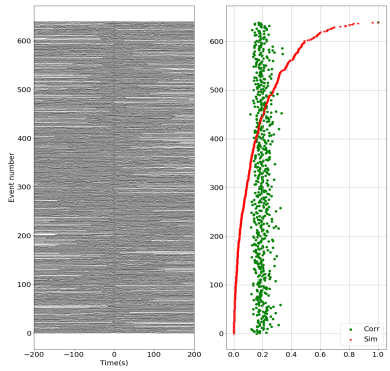

Figure D9. Pressure cluster 6: Same as D5 but for cluster 6.

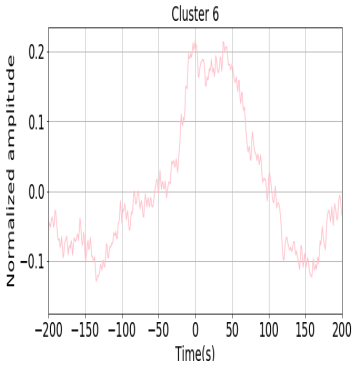

Figure D10. Pressure cluster 6 stack waveform.